Spectral induced polarization of low-pH cement and concrete

Philippe Leroy, Andreas Hördt, Stéphane Gaboreau, Egon Zimmermann, Francis Claret, Matthias Bücker, Hermann Stebner, Johan Alexander Huisman

Spectral induced polarization of low-pH cement and concrete

Philippe Leroy[1*], Andreas Hördt[2], Stéphane Gaboreau[1], Egon Zimmermann[3], Francis Claret[1], Matthias Bücker[2,4], Hermann Stebner[2], Johan Alexander Huisman[5]

[1] Water, Environment and Ecotechnologies Department, Mineralogy, Geochemistry and Modelling of Geological Environments Unit, French Geological Survey, 45060 Orléans, France.

[2] Institute for Geophysics and Extraterrestrial Physics, Technical University Braunschweig, 38106 Braunschweig, Germany.

[3] Electronic Systems, ZEA 2, Central Institute of Engineering, Electronics and Analytics, Forschungszentrum Jülich, 52425 Jülich, Germany.

[4] Research Group Geophysics, Department of Geodesy and Geoinformation, Technical University Wien, 1040 Vienna, Austria.

[5] Agrosphere institute, IBG 3, Institute for Bio- and Geosciences, Forschungszentrum Jülich, 52425 Jülich, Germany.

[*]Corresponding author and mailing address:
Philippe Leroy
D3E/MG2, BRGM
3 Avenue Claude Guillemin
45060 Orléans Cedex 2, France
E-mail: p.leroy@brgm.fr

Published in Cement and Concrete Composites

ABSTRACT

Concrete is the most used material for civil and industrial infrastructures. In the context of a geological disposal of nuclear waste, concrete performance may be degraded when in contact with the host formation. The ability to monitor the changes of the concrete properties using the spectral induced polarization (SIP) method is therefore of great interest. In our study, SIP laboratory measurements in the 100 mHz to 45 kHz frequency range were carried out on low-pH cement and concrete. These materials exhibited a very high resistivity (mostly above 10 kΩ m) and a high phase shift (mostly above 100 mrad) between measured voltage and injected current. The complex resistivity measurements were interpreted using electrochemical and microstructural membrane and Maxwell-Wagner polarization models. Relevant information on the mean pore size, pore size distribution, and connected porosity was obtained from SIP, opening up the possibility of using our approach to monitor concrete stability in-situ.

Keywords: spectral induced polarization; low-pH cement; membrane polarization; Maxwell-Wagner polarization; pore size distribution; connected porosity.

1. Introduction

Since the mid-19th century, the building industry mostly uses Portland cement concrete, which is a composite material made of fine and coarse aggregates embedded in a Portland cement paste containing calcium-silicate-hydrate (C-S-H) [1-4]. Low-pH cement is a mixture of ordinary Portland cement (OPC), pozzolans (such as silica fume, fly ash, and metakaolin) and blast furnace slag [5-8]. In addition to having a low water permeability and long-term durability, other properties of low-pH cement are of particular interest for the storage of high-level and long-lived radioactive waste in deep geological formations [9-12]. The presence of silica-rich pozzolans decreases pore water pH to values below 11 and reduces hydration heat, thus limiting the alkaline attack on the surrounding clayey environment [13-16] and thermal micro-cracking [5, 6, 16, 17], respectively. It also increases compressional strength [18-21] as well as the retention of alkali cations [6, 13, 22, 23].

Mineralogical and microstructural changes of low-pH concrete have been observed in laboratory studies when it was brought in contact with steel reinforcement or other materials (such as bentonite, clay rock or granite) of the geological nuclear waste repository [10-13, 16, 23, 24]. These changes were due to dissolution and precipitation reactions, such as C-S-H dissolution, calcium leaching, and carbonate precipitation, leading to the evolution of the pore space [4, 8, 11, 25]. By changing the surface binding and petrophysical properties of low-pH concrete, such mineralogical and microstructural changes can potentially affect the performance, long-term durability, and confining properties of low-pH concrete [4, 12, 24-26].

In-situ monitoring methods that are fast, non-destructive, and can scan large material volumes are needed to control concrete stability. In the last two decades, the spectral induced polarization (SIP) method has gained popularity in hydrogeophysics to monitor hydraulic properties and biogeochemical changes of soils and rocks for environmental purposes [27-34]. SIP is an impedance spectroscopy (IS) technique where the complex resistivity of the medium is measured with a four-electrode set-up: two electrodes to inject a sinusoidal current in the mHz to kHz frequency range and two electrodes to measure the resulting voltage in the medium [27, 35-38]. Resistivity magnitude and phase shift between measured voltage and injected sinusoidal current are very sensitive to conduction and polarization currents occurring in the bulk aqueous electrolyte and on the wetted surfaces of the pores, hence to the microstructure of the material [34, 37, 39-43]. Compared to impedance spectroscopy with a two-electrode set-up, separation of potential from current electrodes in SIP reduces polarization of potential electrodes, which improves measurement accuracy for frequencies below 1 kHz [38, 44-48].

The low-frequency complex permittivity of cement-based materials is obtained from the measured low-frequency complex impedance, which can be inferred from the SIP method. For frequencies typically below 1 MHz, the permittivity of cement-based materials is influenced by the polarization of the electrical double layer (EDL) on the particle surface (low-frequency process) and by the Maxwell-Wagner polarization due to the charge build-up at the boundaries between solid and liquid materials (higher frequency process) [49-51]. The complex permittivity of cement and concrete is very sensitive to the salinity, the pore size distribution as well as the connected porosity and water saturation and hence can be used to monitor cement hydration and durability, and moisture and chloride ingress in cement [49-56]. Studies showed that the salinity

increases the low-frequency permittivity of cement-based materials and that small pores have a tendency to increase the permittivity at higher frequencies than larger pores. It has also been observed that the permittivity decreases during cement hydration and when the water to cement ratio decreases because of the reduction of the (electrically) connected porosity and that the cement permittivity decreases when the water saturation decreases.

Previous laboratory studies focused on the impedance of cementitious materials have mostly used a two-electrode set-up as typically done in impedance spectroscopy studies [52, 57-62]. Their measurement accuracy at low frequencies (typically < 1 kHz) was limited due to electrode polarization. Some impedance spectroscopy measurements on cement-based materials have been carried out using a four-electrode set-up to diminish electrode polarization [63-67]. Recently, Smyl et al. [68, 69] also successfully used at the laboratory the Electrical Impedance Tomography (EIT) method (a multi-electrode array system) to image in three dimensions the distribution of electrical conductivity at a frequency of 40 kHz and the moisture ingress in undamaged and damaged Portland cement mortars.

Many previous studies on resistivity measurements for cementitious materials used equivalent circuit models to derive from the geophysical measurements the sample microstructural and petrophysical properties, such as the pore structure and connected porosity, and the related transport properties (permeability, diffusivity). However, such circuit models are only phenomenological in nature and are not based on the equations describing ion transport in charged porous media under the influence of the applied electric field, i.e. the Poisson-Nernst-Planck (PNP) equations [70-75]. In hydrogeophysics, membrane polarization models based on the PNP equations have been

developed to determine the frequency-dependent normalized impedance due to the difference in ion selectivity between active (ion selective) and passive (ion non selective) zones [42, 76-81]. Bücker and Hördt [42] modified the 1D membrane polarization model of Marshall and Madden [76] to compute the normalized impedance of a bi-tube system resulting from the difference in ion selectivity between narrow and wide pores due to the EDL on their surface (counter-ion adsorption and co-ion repulsion). The membrane polarization model of Bücker and Hördt [42] was recently extended to take into account the porosity [82], the pore size and length distribution [83], and Maxwell-Wagner polarization [84] [85, 86].

To the best of our knowledge, there are no impedance spectroscopy measurements on low-pH cement and concrete interpreted by a membrane polarization model. In our study, the SIP system developed by Zimmerman et al. [38] was used to measure the impedance of these materials in the low-frequency range (100 mHz-45 kHz). These SIP measurements were then interpreted using the extended membrane polarization models of Bairlein et al. [82] and Stebner et al. [83] to consider Maxwell-Wagner polarization [84] and the interlayer spaces of C-S-H. The first part of our manuscript presents the material properties as well as the SIP experimental set-up. The second part briefly explains the microstructural and electrochemical properties of C-S-H and cement as well as the extended membrane polarization models. Finally, the third part shows the SIP measurements and their interpretation in terms of mean pore radius and length, pore radius and length distributions, and connected porosity.

2. Materials and methods

2.1. Sample preparation and chemical composition

Hydrated cement paste (HCP) and concrete samples were cured under a plastic sheet for 91 days in a laboratory at a temperature of 23°C and a relative humidity of 95%. The samples were then immersed in equilibrium water for one year in a closed container to ensure full cement hydration. The pH was measured at 11.5 ± 0.2. The diameter of both cylindrical samples is 5 cm and the lengths of the cement and concrete samples are 10 and 20 cm, respectively. The chemical compositions of HCP and concrete are listed in Table 1. Samples are a mixture of CEM I Portland cement with silica fume, blast furnace slag, quartz sand, and added quartz-rich aggregates (granites) for concrete. CEM I mostly contains CaO (~67.5 weight %) and SiO_2 (~22.5 wt %), hence has three CaO for one SiO_2 compound ($3CaO•SiO_2$), and C-S-H with a Ca/Si ratio of 1.7 [6, 87]. Silica fume and quartz contain at least 95 wt % of SiO_2, and blast furnace slag contains 42 wt % of CaO, 36 wt % of SiO_2, 11 wt % of Al_2O_3, and 8 wt % of MgO [2, 6]. The water-to-binder ratio, i.e. the ratio of the weight of water to the weight of cement, is 0.25 for HCP and 0.43 for concrete.

Table 1

Chemical composition of the samples (kg m^{-3}).

Materials	Paste	Concrete
CEM I 42.5[a]	468	105
Silica fume	491	110
Blast furnace slag	290	65
Quartz filler	517	116
Aggregates 0-1 mm	-	168
Aggregates 1-8 mm	-	770
Aggregates 8-16 mm	-	532
Aggregates 16-32 mm	-	396
Water (effective)	312	120
Superplasticizer	75	16.80
Water/binder ratio	0.25	0.43

[a] Resistance to compressive strength in MPa after 28 days.

2.2. Sample petrophysical properties

Prior to the petrophysical measurements, HCP and concrete samples were heated at 100°C for 36 hours and cooled under vacuum conditions to ensure that all water left the pores. Total porosities of the samples were calculated according to

$$\phi = 1 - \rho / \rho_g , \quad (1)$$

where ρ is the apparent dry density inferred from mercury intrusion porosimetry (MIP) or kerosene porosity (KP) (g cm^{-3}) and ρ_g is the solid grain density measured with a Micromeritics® Accupyc 2020 helium pycnometer (HP) (Table 2, more details are given in Gaboreau et al. [88]). Estimated porosities were around 25 and 12.5% for HCP and concrete, respectively. Using:

$$\phi_{\mathrm{MIP}} = V_{\mathrm{Imax}}\rho\,, \tag{2}$$

where V_{Imax} is the maximum intruded volume of mercury ($cm^3\ g^{-1}$), we found that only ~25% and 30% of the HCP and concrete pore volumes were probed by MIP, respectively. This means that most of the pores in HCP and concrete have pore-throat sizes below 7 nm because mercury cannot penetrate these small pore throats [89].

Table 2

Measured densities ($g\ cm^{-3}$) and estimated porosities (%) of the two materials.

	Dry density ρ		Grain density ρ_g	Porosity ϕ		
Methods	MIP	KP	HP	MIP	KP	Calculated[a]
HCP	1.878	1.830	2.48	6.07	26.21	24.3
Concrete	2.275	2.284	2.61	3.8	12.47	12.8

[a] According to Eq. (1) and density measurements.

Mercury intrusion curves were inferred from the Micromeritics® Autopore IV 9500 apparatus by increasing pressure from 0.1 to 200 MPa on 2 cm^3 samples immersed in mercury. The pressure required to intrude mercury into the pores is inversely proportional to the pore-throat diameter. Cumulative (Fig. 1a) and incremental (Fig. 1b) pore-throat size distributions were calculated from the intrusion curves assuming cylindrical pores and using Washburn's law with a contact angle of 141.3° [90]. Pore volume curves were expressed in percentage of the total pore volume to illustrate the fractions of the pore volume probed by mercury. For both materials, the main pore-throat size is around 13 nm. Two other main pore-throat sizes were detected around 1 µm and beyond 100 µm, the latter one being mainly due to sample surface roughness.

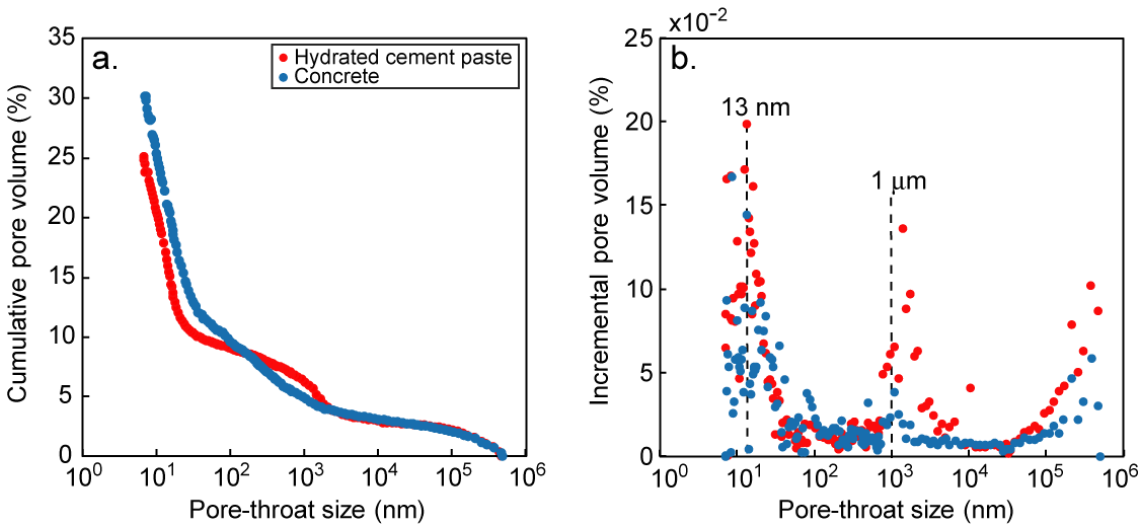

Fig. 1. a. Cumulative and b. incremental MIP curves for HCP and concrete.

2.3. Experimental set-up for SIP measurements

Impedance measurements in the 100 mHz to 45 kHz frequency range were carried out on cylindrical HCP and concrete samples removed from the storage container. The room temperature during the experiment was 21 ± 0.5 °C. To do the SIP measurements, the ZEL-SIP-04 system (Fig. 2a) developed by Zimmermann et al. [38] and built at Forschungszentrum Jülich GmbH, Germany, was connected to a sample holder specifically designed for cementitious materials (Fig. 2b). The SIP system consists of a function generator (Agilent 33120A), a measurement amplifier, an Analog-to-Digital Converter (ADC) card, and a PC-based measurement control system [38, 45]. The function generator produces a sinusoidal ± 5 V voltage to inject a low sinusoidal current (in the µA range) into the sample [38, 45]. Porous bronze plates were used as current electrodes. A sinusoidal voltage resulting from the current flow in the sample was measured with two potential electrodes, which were brass cylinders of diameter 6 mm. Synthetic sponges wetted with the equilibrium water from the storage container were used

to ensure contact between the electrodes and the sample. For the HCP sample, current and potential electrodes were separated by a distance of 24 and 6 cm, respectively. For the longer concrete sample, these separation distances were 30 and 12 cm, respectively.

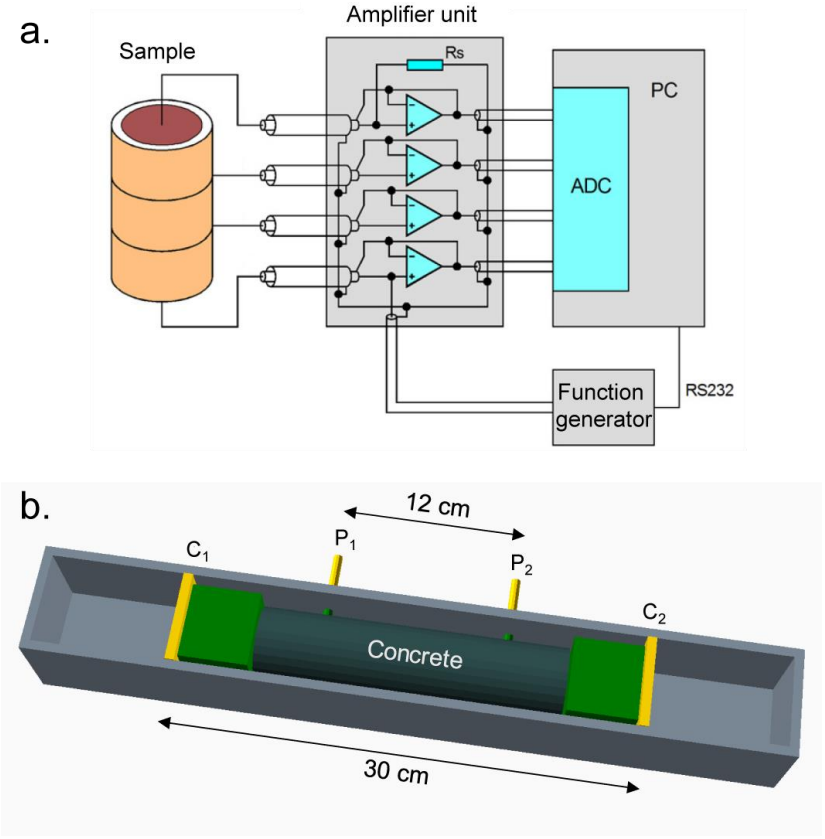

Fig. 2. a. Sketch of the ZEL-SIP-04 system (modified, from Zimmermann et al. [38]). b. Sketch of the sample holder for SIP measurements on concrete. Synthetic wet sponges (light green) were used to establish contact between the current (C_1, C_2) and potential (P_1, P_2) electrodes and the sample (dark green).

Measured sample impedance Z_o^* (Ω) (subscript "*o*" for observed) is a complex quantity and was determined by the ratio between the measured output voltage U^* (V) and input current I^* (A):

$$Z_o^*(\omega) = \frac{U^*}{I^*} = \left|Z_o^*(\omega)\right| e^{j\varphi(\omega)}, \quad (3)$$

where ω is the angular frequency (rad s^{-1}) ($\omega = 2\pi f$ with f being the frequency in Hertz), j is the imaginary number ($j^2 = -1$), and φ is the phase shift between the voltage and current (rad). The measured complex resistivity $\rho_o^*(\omega)$ (Ω m) is related to the measured complex impedance by a cell constant k (m^{-1}), $\rho_o^*(\omega) = Z_o^*(\omega) / k$. This cell constant was calculated using $k = l / S$, where l is the distance between the two potential electrodes (m) and S is the cross-sectional area of the cylindrical sample holder (m^2) [46, 91-93]. For the HCP and concrete samples, the cell constant was calculated as ~30.5 and ~61 m^{-1}, respectively, considering a distance l of 6 and 12 cm, respectively, and a cross-sectional area S of 19.63 cm^2 for a cylinder radius r of 2.5 cm ($S = \pi r^2$).

Preliminary SIP measurements indicated a high resistivity for both HCP and concrete samples. The measured impedance was in the range of 1 MΩ, a range where the used SIP system has not been properly tested before. Therefore, initial test measurements were carried out on a reference electrical circuit that mimics the properties of the measurement set-up for the HCP and concrete samples. A sample resistance of 909 kΩ with a nominal accuracy of 1% was selected and realistic contact impedances for both the current (332 kΩ) and potential electrodes (619 kΩ) were considered in the reference electrical circuit. The uncorrected SIP measurement depicted in Fig. 3a (red squares) shows that the measured impedance magnitude corresponds well with the expected resistance of 909 kΩ. The zoom provided in Fig. 3b shows that the measured impedance falls within the reported accuracy of the resistance used within the reference electrical circuit. The measured phase shift starts to deviate from zero at approximately 100 Hz (Fig. 3c). This is due to the measurement errors associated with the contact impedance of the potential electrodes and the remaining leaking currents in the SIP system and experimental set-up [45]. At 1 kHz, the measurement error without correction amounted to 30 mrad. After

correction for the contact impedance of the potential electrodes using the method outlined in Huisman et al. [45], this error was reduced to 10 mrad. The close-up provided in Fig. 3d indicates that the measurement error for the phase shift is approximately 1 mrad for frequencies below 100 Hz. These errors are higher than those previously reported for this SIP measurement system [38, 46, 94, 95]. This is related to the challenges associated with making accurate measurements on highly resistive samples. The results of this test measurement were used to evaluate the significance of the SIP measurements on HCP and concrete samples.

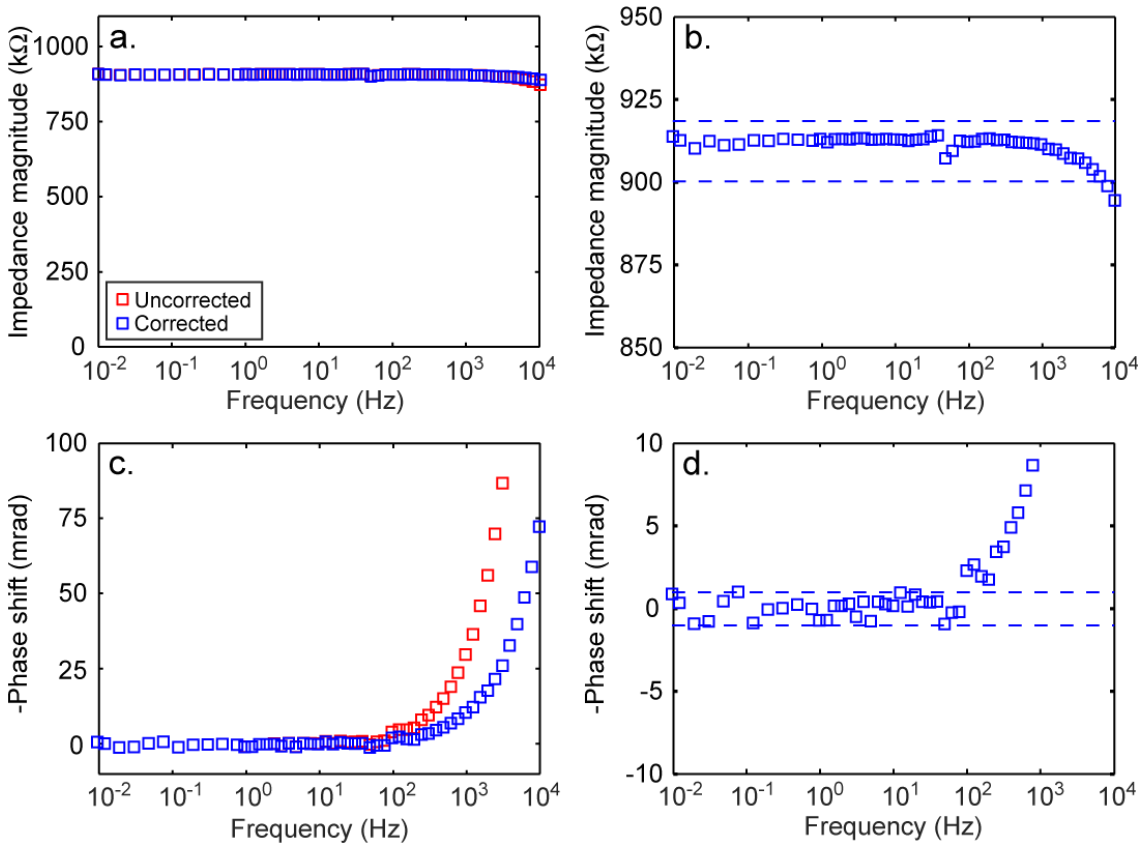

Fig. 3. Complex impedance measurements on a reference electrical circuit. Ideally, the magnitude of the measured impedance should be 909 kΩ with zero phase shift.

3. Theory

3.1. C-S-H microstructural and electrochemical properties

Most of the volume of hydrated cement is occupied by the C-S-H phase, which controls the chemical, physical, and mechanical properties of cement [96-99]. Dynamic small-angle neutron scattering (SANS) [100, 101] and atomic force microscopy (AFM) [102] measurements showed that the average thickness of lamellar C-S-H particles is on the order of 5 nm. Gauffinet et al. [102] used AFM measurements to determine the dimensions of C-S-H crystallites, which were found to be 60×50×5 and 60×30×5 nm^3 for Ca/Si ratios between 1 – 1.5 and 1.7 – 2.0, respectively. Solid-state nuclear magnetic resonance (NMR) and X-ray diffraction (XRD) studies revealed the structure and chemical composition of the solid sheets constituting C-S-H particles (Fig. 4a) [103, 104]. It was found that the solid layers within the particles consist of three sheets, a "pseudo-octahedral" calcium plane between two tetrahedral silicate chains. The silicate chains form dreierketten structures with two paired tetrahedra and one bridging tetrahedron. Bridging silicates progressively disappear when the Ca/Si ratio increases from 0.67 to 1.5 [97]. The solid layers inside the particle are separated by interlayer spaces containing water molecules and calcium ions that compensate the negative surface charge. According to crystallography [105], gas (nitrogen) and water adsorption isotherms [106], and NMR, SANS and small-angle X-ray scattering (SAXS) measurements [107], the specific surface area of a C-S-H particle is equal to $500/n_s$ m^2 g^{-1}, where n_s is the number of solid layers per particle ($1 \leq n_s \leq 4$).

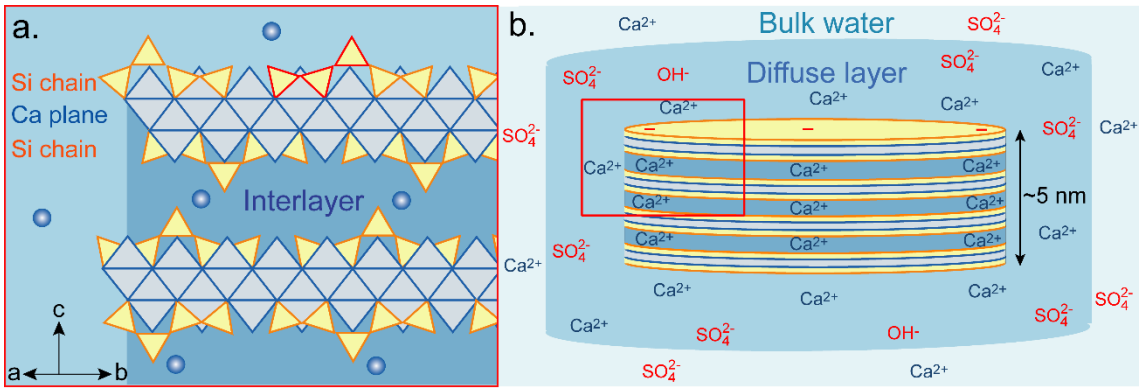

Fig. 4. a. Close-up of a C-S-H particle in a calcium sulfate aqueous electrolyte. The dreierketten structure of the silicate chains is drawn in red (modified, from Grangeon et al. [108]). b. Diffuse layer around the C-S-H particle containing calcium cations in excess and sulfate anions in deficiency to compensate the external negative surface charge of C-S-H (modified, from Haas and Nonat [105]).

Due to their high specific surface area and external surface charge, C-S-H particles may control the electrical response of HCP and concrete. In the following, we will use the words “surface charge” for the external surface charge of C-S-H. The surface charge of C-S-H originates from the negative charge due to the deprotonation of the silanol sites on the silicate tetrahedra and from the positive charge due to the preferential adsorption of calcium cations [96]. The surface charge forms an electrical double layer around the C-S-H particle attracting counter-ions and repulsing co-ions in the electrical diffuse layer (Fig. 4b) [96, 109, 110]. The thickness of the diffuse layer is in the nanometer range and it can therefore control ion selectivity in cement micropores [111]. A compact Stern layer exclusively containing counter-ions may also be located closer to the C-S-H surface to compensate its surface charge. However, in our study, we will not go into further details on the Stern layer because, to the best of our knowledge, this layer has not been clearly

described for C-S-H and the calcium ions in the Stern layer may have a very low mobility (a discussion regarding this point is presented at section 3.2),

The surface charge of C-S-H cannot be measured by conventional techniques such as acid-base potentiometric titration because of the high chemical reactivity of C-S-H that has an equilibrium pH > 10 [112]. For that reason, electrophoresis is the method usually used to indirectly obtain information on the surface charge of C-S-H [96, 99, 105, 109, 110, 112]. However, this method is sensitive to the zeta potential, which is the electrical potential at the shear plane located at a certain distance (in the nanometer range) from the surface [113-121]. According to the sign of the measured electrophoretic mobility and zeta potential, the surface charge may be negative for a C-S-H particle with a low Ca/Si ratio, typically ≤ 1, whereas it may be positive for higher Ca/Si ratios [96, 99, 105]. In our study, C-S-H particles have a low Ca/Si ratio due to the addition of silica-based materials to obtain low-pH cement and therefore their surface charge is probably negative [6, 13, 22, 23]. This implies that the diffuse layer of C-S-H may attract calcium cations and repulse sulfate anions.

3.2. Pore structure of cement-based materials and ion selective properties

Cementitious materials have a complex pore structure because they are composed of different types of grains and particles, from nanometric C-S-H particles to micrometric or millimetric carbonate or silicate-rich grains (Figs. 5a,b) [2, 4-6, 16, 88, 106]. The pores of cement-based materials are usually classified into four types of pores. There are the C-S-H interlayer spaces of thickness ≤ 2 nm, the gel pores, which are micropores of widths

between ~2 and 8 nm, the capillary pores, which are mesopores with diameters ranging from ~8 nm to 10 µm, and the macropores of sizes larger than 10 µm due to deliberately entrained air and inadequate compaction [4, 111, 122]. Macro- and mesopores with low ion selectivity connected with micropores with high ion selectivity may be responsible for a membrane polarization effect that increases cement polarization for low-frequencies of injected current (this effect will be explained in more detail in section 3.3). Like for hydrated montmorillonite, the interlayer spaces of C-S-H may be very resistive because the adsorbed calcium cation may have a very low mobility and thus may not contribute significantly to conduction currents [123-125].

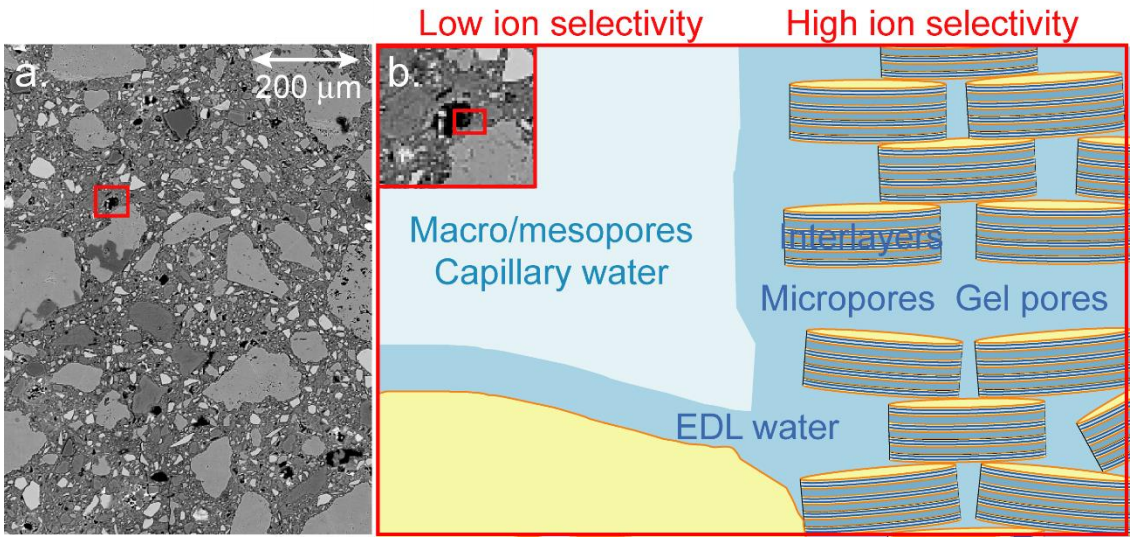

Fig. 5. a. Backscattered electron (BSE) image of low-pH cement (modified, from Gaboreau et al. [8]). The brightest parts represent the highest Ca weight %, the anhydrous phases appear in light gray, the hydraulic binder (mostly C-S-H) and silica grains appear in dark gray, and the macropores appear in black. b. Close-up of the pore structure of low-pH cement showing the zones with low and high ion selectivity (modified, from Jennings [101]).

3.3. Combined membrane and Maxwell-Wagner polarization model

We used extensions of the membrane polarization (MP) model suggested by Bücker and Hördt [42] to explain the SIP measurements on HCP and concrete. This model is based on the equation of Marshall and Madden [76] for the normalized impedance of a porous medium consisting of a sequence of two types of one-dimensional pores with different ion mobility (Fig. 6a). The zones have different transport numbers for cations and anions, which produce local concentration gradients in the presence of an applied external electric field (Fig. 6b). The local solute flows, appearing due to these concentration gradients, result in additional electrical current in ion selective zones. This in turn yields an additional electrical field and causes the frequency dependency of the normalized impedance. Bücker and Hördt [42] extended the 1D impedance model of Marshall and Madden [76] to an impedance model for a 2D system where the two pore types consist of cylinders with different radii and lengths. In contrast to the model of Marshall and Madden [76], ions have the same mobility in the two pore types in the model of Bücker and Hördt [42] (Figs. 6c,d). Instead, the ion selective properties of the pores, which control electrical conduction and polarization, are determined by the EDL properties (counter-ion attraction and co-ion repulsion) described by the zeta potential (ζ) and the fraction of the counter-charge located in the Stern layer (f_Q) [113-115, 126-129].

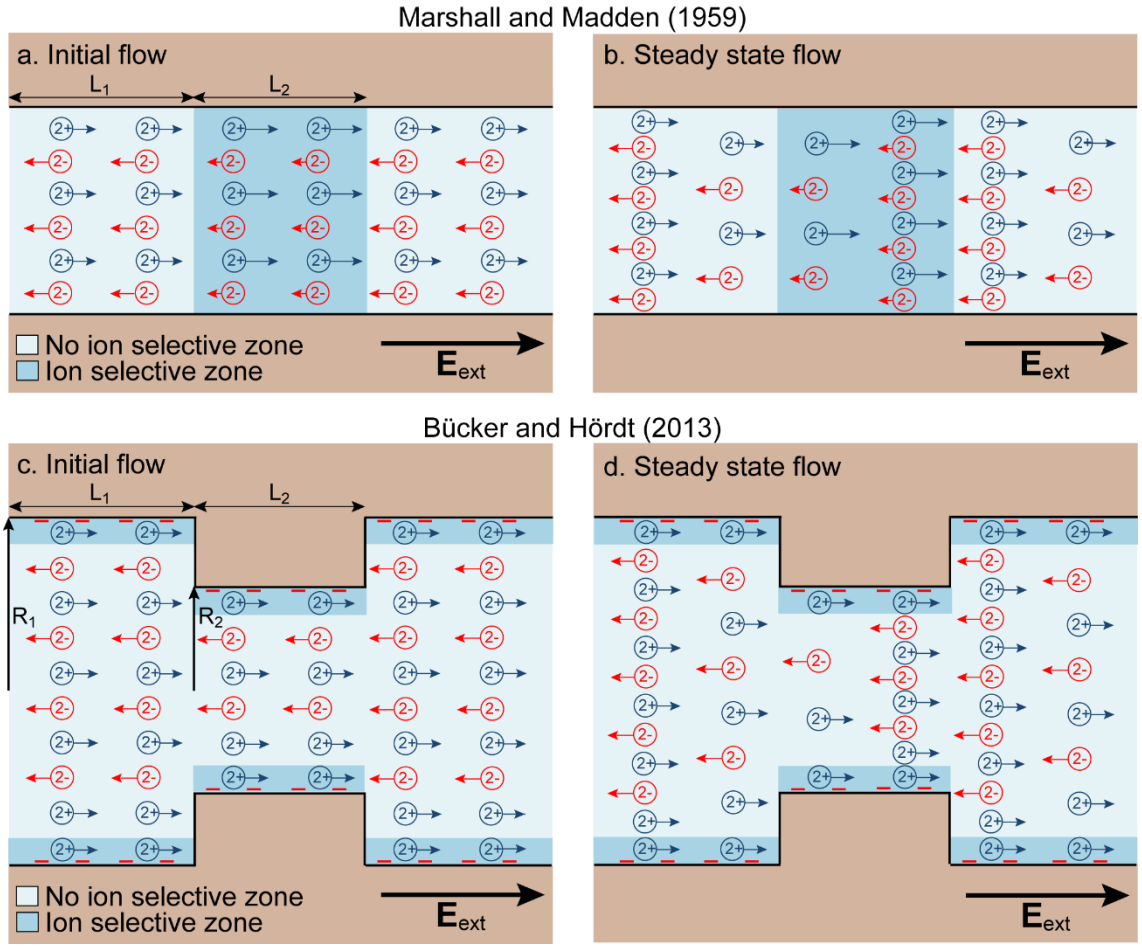

Fig. 6. Sketch of the membrane polarization model of Marshall and Madden [76] (a, b) and Bücker and Hördt [42] (c, d) when the porous medium containing a $CaSO_4$ aqueous electrolyte is under the influence of the external electric field $\mathbf{E}_{ext}$. In steady state conditions, ion concentration gradients due to the ion selectivity in the membrane zone appear. The length of the arrow depicted for the ions denotes the magnitude of the ion mobility.

Marshall and Madden [76] analytically solved the Poisson-Nernst-Planck equations, which are nonlinear partial differential equations, to describe ion electromigration and diffusion in the porous medium under the influence of a sinusoidal electric field in the mHz to kHz frequency range. However, their analytical solution for the normalized

impedance is restricted to 1:1 aqueous electrolytes (such as NaCl or KCl) and the pore water of low-pH cement contains a mixture of divalent and monovalent ions such as Ca^{2+}, SO_4^{2-}, OH^-, Na^+ and K^+ ions [6, 130]. An extension of their theory to complex aqueous electrolytes is not trivial, and was not carried out so far. However, the theory of Marshall and Madden [76] can be easily extended to a binary symmetric electrolyte of valence *z* by replacing the Faraday constant *F* by *zF* in their ion transport equations. In the pore water of low-pH cement, Ca^{2+} and SO_4^{2-} ions usually have higher concentrations and have a higher electrical charge than OH^-, Na^+ and K^+ ions [13, 14]. Therefore, their influence on electrostatic phenomena controlling water electrical conductivity and membrane polarization may be higher. For this reason, we considered that the pore water of HCP and concrete contains a calcium sulfate electrolyte. This allowed us to simulate the normalized impedance (Ω m^2) of our samples using a simple modification of the original Marshall and Madden [76] model considering the valence $z = 2$ and concentration c_0 of the $CaSO_4$ electrolyte:

$$\overline{Z}^*_{MP}(\omega) = \frac{L_1}{\mu_p \tilde{b}_{p1} c_0 zF}\left[\tilde{t}_{p1} + \frac{\tilde{B}}{A}\tilde{t}_{p2} + \frac{\left(\tilde{S}_2 - \tilde{S}_1\right)^2}{\frac{\tilde{X}_1(\omega)\tilde{S}_1}{\tilde{t}_{p2}^2 \tilde{t}_{p1}\tanh\left(\tilde{X}_1(\omega)\right)} + \frac{A}{\tilde{B}}\frac{\tilde{X}_2(\omega)\tilde{S}_2}{\tilde{t}_{p1}^2 \tilde{t}_{p2}\tanh\left(\tilde{X}_2(\omega)\right)}}\right], \qquad (4)$$

where L_1 is the wide pore length (m) (Figs. 6a,c and Fig. 7a), *F* is the Faraday constant (~96485 C mol^{-1}), and μ_p is the mobility (m^2 s^{-1} V^{-1}), $\tilde{b}_{pi}$ is the normalized concentration, and $\tilde{t}_{pi}$ is the transference number of the cations (subscript "*p*" for positive charge) in the pore type *i*. The cation transference number is a key parameter in Eq. (4) because it represents the fraction of the electrical current carried by the cation and cation selectivity ($\tilde{t}_{pi} + \tilde{t}_{ni} = 1$ where $\tilde{t}_{ni}$ is the anion transference number):

$$\tilde{t}_{pi} = \frac{\mu_p \tilde{b}_{pi}}{\mu_p \tilde{b}_{pi} + \mu_n \tilde{b}_{ni}}, \quad (5)$$

where μ_n is the mobility and $\tilde{b}_{ni}$ is the normalized concentration of anions (subscript "*n*" for negative charge) in the pore type *i*. Both $\tilde{b}_{pi}$ and $\tilde{b}_{ni}$ depend on the pore radii and EDL properties (ζ, f_Q) (Eqs. (A7) to (A12) in Appendix A). According to Eq. (5), $0 \le \tilde{t}_{pi} \le 1$. When $\tilde{t}_{pi} = 0$, cations are excluded from the pore *i* ($\tilde{b}_{pi} = 0$) and when $\tilde{t}_{pi} = 1$, anions are excluded ($\tilde{b}_{ni} = 0$). When $\tilde{b}_{pi} = \tilde{b}_{ni}$, there is no ion selectivity and the cation transference number in pore *i* corresponds to the cation microscopic Hittorf number $t_p = \mu_p / (\mu_p + \mu_n)$ [131]. The remaining parameters in Eq. (4) are explained in Appendix A.

The normalized impedance model of Bücker and Hördt [42] requires therefore chemical, electrochemical, and geometrical input parameters (electrolyte concentration and valence, ion mobilities, zeta potential, fraction of the counter-charge in the Stern layer, and two pore radii and lengths). In the following, we will only consider diffuse layer influence on ion selectivity, i.e. $f_Q = 0$ in the model of Bücker and Hördt [42]. To include the connected porosity ϕ_c in our membrane polarization model, we used the approach described in Bairlein et al. [82]. It considers a cylindrical, non-conducting matrix encompassing the pore system (Fig. 7a) to convert modelled normalized impedance $\bar{Z}^*_{MP}$ into effective conductivity σ^*_{MP} (S m^{-1}) using

$$\sigma^*_{MP} = \frac{A_1}{\bar{Z}^*_{MP}} \frac{L_a{}^2 \phi_c}{A_1 L_1 + A_2 L_2}, \quad (6)$$

where A_i is the cross-sectional area of the cylindrical pore *i* (m^2) and L_a is the total length of the two pores, $L_a = L_1 + L_2$ (m).

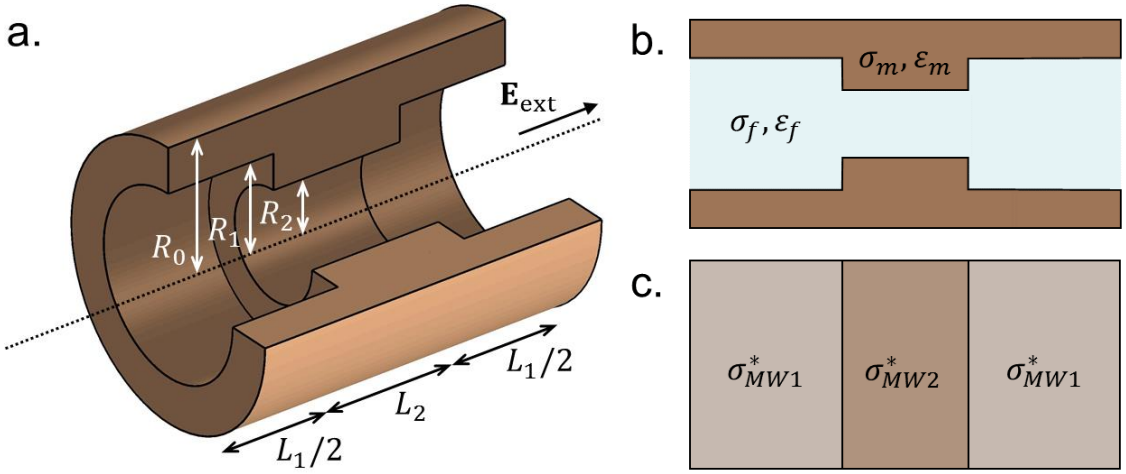

Fig. 7. a. Cylindrical model consisting of the wide pore (length L_1, radius R_1), narrow pore (length L_2, radius R_2) and non-conducting matrix (thickness $R_0 - R_1$ or $R_0 - R_2$). b. Cross-section through the pore system showing the pore and surrounding matrix conductivity and permittivity. c. Reduction of b. to a layered medium with effective complex Maxwell-Wagner conductivities (after Bücker [84]).

An additional polarization mechanism named Maxwell-Wagner (MW) polarization may be relevant for the explanation of the SIP measurements, especially for the kHz frequency range [85, 132]. MW polarization is a charge build-up process occurring at the boundary between two dielectric media with different electrical properties (conductivity and permittivity) [126]. In complex conductivity models based on EDL polarization around grains, MW polarization is considered during the upscaling procedure when the conductivity of the porous medium is computed from the conductivities of the aqueous electrolyte and grains using for instance the Bruggeman-Hanai-Sen (BHS) model based on the differential effective medium (DEM) theory [34, 39, 40, 117, 133]. Here, we used an alternative approach adapted to the membrane polarization model to simulate MW polarization (Figs. 7b,c) [84]. In this approach, the 2D capillary (bi-tube) system was first

reduced to a 1D system by calculating the effective conductivity per section assuming that the conductivities of the fluid (subscript "*f*") and matrix (subscript "*m*") are connected in parallel. Therefore, the conductivities were simply averaged using weights based on their cross-sectional fractions. We obtained:

$$\sigma^*_{MWi} = \frac{R_i^2}{R_0^2}\sigma^*_f + \frac{R_0^2 - R_i^2}{R_0^2}\sigma^*_m, \tag{7}$$

with

$$\sigma^*_{f,m}(\omega) = \sigma_{f,m} + j\omega\varepsilon_{f,m}, \tag{8}$$

where the subscript "*i*" denotes the wide (i =1) or narrow pore (i =2) and $\varepsilon_{f,m} = \varepsilon_{rf,m}\varepsilon_0$ is the absolute permittivity (F m^{-1}) with $\varepsilon_{rf,m}$ being the relative and ε_0 the vacuum (~8.854×10^{-12} F m^{-1}) permittivity. In Eq. (8), following Maxwell's equations and Ohm's law, we considered that the fluid (here water in the pores) and matrix complex conductivities result from the sum of Ohmic and dielectric displacement currents represented by electrical conductivity and permittivity, respectively [133].

In a second step, the MW conductivity of the bi-tube system surrounded by the matrix was obtained by adding the reciprocals (i.e. the resistivities) of the two sections connected in series – now weighted by their lengths:

$$\frac{L_1 + L_2}{\sigma^*_{MW}} = \frac{L_1}{\sigma^*_{MW1}} + \frac{L_2}{\sigma^*_{MW2}}, \tag{9}$$

thus we obtained

$$\sigma^*_{MW} = \frac{L_a\sigma^*_{MW1}\sigma^*_{MW2}}{L_1\sigma^*_{MW2} + L_2\sigma^*_{MW1}}. \tag{10}$$

In our approach, the MW effective conductivity is considered a conduction mechanism that acts in parallel to the membrane polarization conductivity σ^*_{MP} calculated according

to Bairlein et al. [82] (Eq. (6)). To compute the effective conductivity of the bi-tube system and the insulating matrix considering both MP and MW polarization, we substituted the low-frequency limit of the MW conductivity $\sigma^*_{MW}(\omega \to 0)$ by σ^*_{MP}, i.e.

$$\sigma^*_{eff} = \sigma^*_{MW} - \sigma^*_{MW}(\omega \to 0) + \sigma^*_{MP} . \quad (11)$$

From this new effective conductivity, we calculated the frequency-dependent effective resistivity $\rho^*_{eff} = 1/\sigma^*_{eff}$ and phase shift φ ($-\varphi = \tan^{-1}(\sigma''/\sigma')$ with $\sigma^*_{eff} = \sigma' + j\sigma''$), which were compared to the measured SIP data.

In order to match the SIP measurements quantitatively, a trial-and-error approach was used where some of the model parameters were fixed or constrained to certain ranges while others were freely varied to achieve a good data fit. Existing knowledge about the behaviour of membrane polarization entered into the procedure. For example, Hördt et al. [134] have shown that the frequency at which the maximum magnitude of the phase shift occurs is controlled by the length of the wide pore. They also gave simple relationships between pore radii and lengths that provide maximum phase shift magnitudes. In our study, we adjusted the geometrical parameters (pore radii and lengths and matrix radius) to match the measured SIP spectra. The values of the other model parameters are listed in Table 3.

Table 3

Parameter values of the combined membrane and MW polarization model (excluding the geometrical parameters).

Property	Symbol	Value
Matrix conductivity	σ_m	0 S m^{-1}
Relative matrix permittivity	ε_{rm}	4.5
Relative fluid permittivity	ε_{rf}	80
Calcium ion mobility	μ_p	5.6×10^{-8} m^2 s^{-1} V^{-1}
Sulfate ion mobility	μ_n	7.6×10^{-8} m^2 s^{-1} V^{-1}
Bulk electrolyte concentration	c_0	3.5 mol m^{-3}
Bulk electrolyte valence	z	2
Fluid conductivity	σ_f	0.086 S m^{-1}
Zeta potential	ζ	–40mV
Partition coefficient	f_Q	0

The relative permittivity of the matrix was estimated from values reported in the literature for non-conducting materials [135]. The relative permittivity of the fluid was taken from a value reported in the literature for water at a temperature of 21°C corresponding to the mean temperature during SIP measurements [136]. Ion mobility at a temperature of 21°C was calculated from the measured ion diffusion coefficient at a temperature of 25°C reported in the PHREEQC database file phreeqc.dat [137] corrected for temperature using the model of Leroy et al. [46] (their Eq. (15)) and the Nernst-Einstein equation (Eq. (A6)). To obtain information on the bulk electrolyte concentration c_0, the resistivity of the equilibrium water in the storage container was measured. It was found to be 11.6 Ω m at a temperature of 21°C, corresponding to an electrical conductivity of 0.086 S m^{-1}. According to the Kohlrausch's law for diluted electrolytes [138], water conductivity was computed as a function of c_0 using

$$\sigma_f = 2F(\mu_p + \mu_n)c_0. \quad (12)$$

Using Eq. (12), measured σ_f value and ion mobilities (Table 3), we obtained a c_0 concçentration of 3.5 mol m^{-3} for our normalized impedance model. A zeta potential of –40 mV was assumed according to values reported in the literature for C-S-H with a low Ca/Si ratio ≤ 1 as is the case for low-pH cement [96, 99, 112, 139, 140]. The partition coefficient of the counter-charge in the Stern layer was set to zero because of the lack of detailed information in the literature about this layer at the C-S-H surface and also because surface-adsorbed calcium ions may have a very low mobility and then may marginally contribute to electromigration and diffusion [105, 123].

4. SIP measurements and interpretation

Three different impedance models were considered to interpret SIP spectra of HCP and concrete in terms of pore radii, lengths, and (electrically) connected porosity, while fixing the chemical and electrochemical parameters (Table 3). There are (1) a single bi-tube system (covered by the insulating matrix), (2) a bi-tube network model using the approach of Stebner et al. [83], and (3) two bi-tube systems in parallel (Fig. 8). Before using the impedance models to interpret the SIP measurements, the measured resistivity magnitudes were described by Archie's first law and the measured phase shifts were discussed.

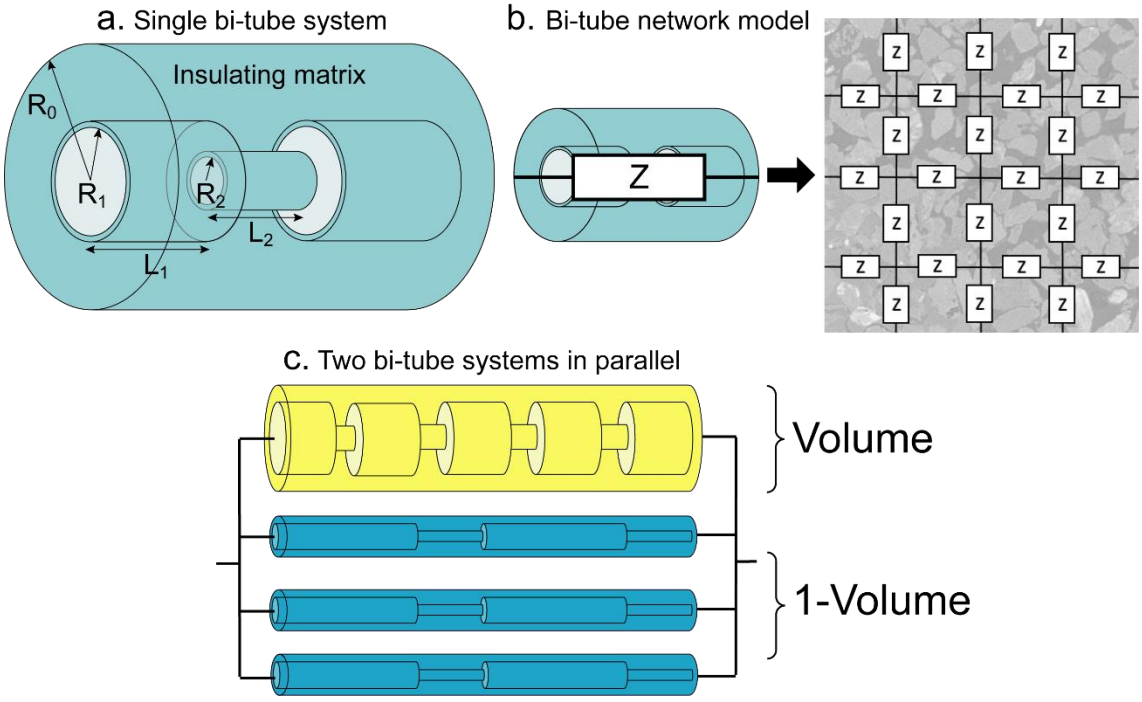

Fig. 8. Impedance models to interpret HCP and concrete SIP spectra.

4.1. SIP measurements

The measured resistivity magnitudes of HCP and concrete are extremely high with values above 1 kΩ m and decrease with increasing frequency due to polarization mechanisms such as membrane and MW polarization (Figs. 9a,c). These high resistivity magnitudes are surprising at first glance because the bulk pore water resistivity is likely relatively low (the measured resistivity of the water surrounding the samples in the storage box was 11.6 Ω m) and the measured sample porosities are relatively high (~25% for HCP and ~12.5% for concrete, Table 2). Interestingly, for frequencies below 1 kHz, the HCP resistivity magnitude is ~1.7 times the concrete resistivity magnitude despite the fact that the HCP porosity is about twice as high. The observed resistivity difference can be explained by the difference in the binder content of the two samples. HCP and concrete

have a binder-to-water ratio of 4.0 and 2.3 (Table 1), respectively. Hence, their binder ratio is ~1.7, the same ratio as for resistivity. C-S-H has a high specific surface area (between ~125 and 500 m^2 g^{-1}) and occupies most of the volume of hydrated low-pH cement [8]. Therefore, the extremely high HCP and concrete resistivities can be explained by their high C-S-H content.

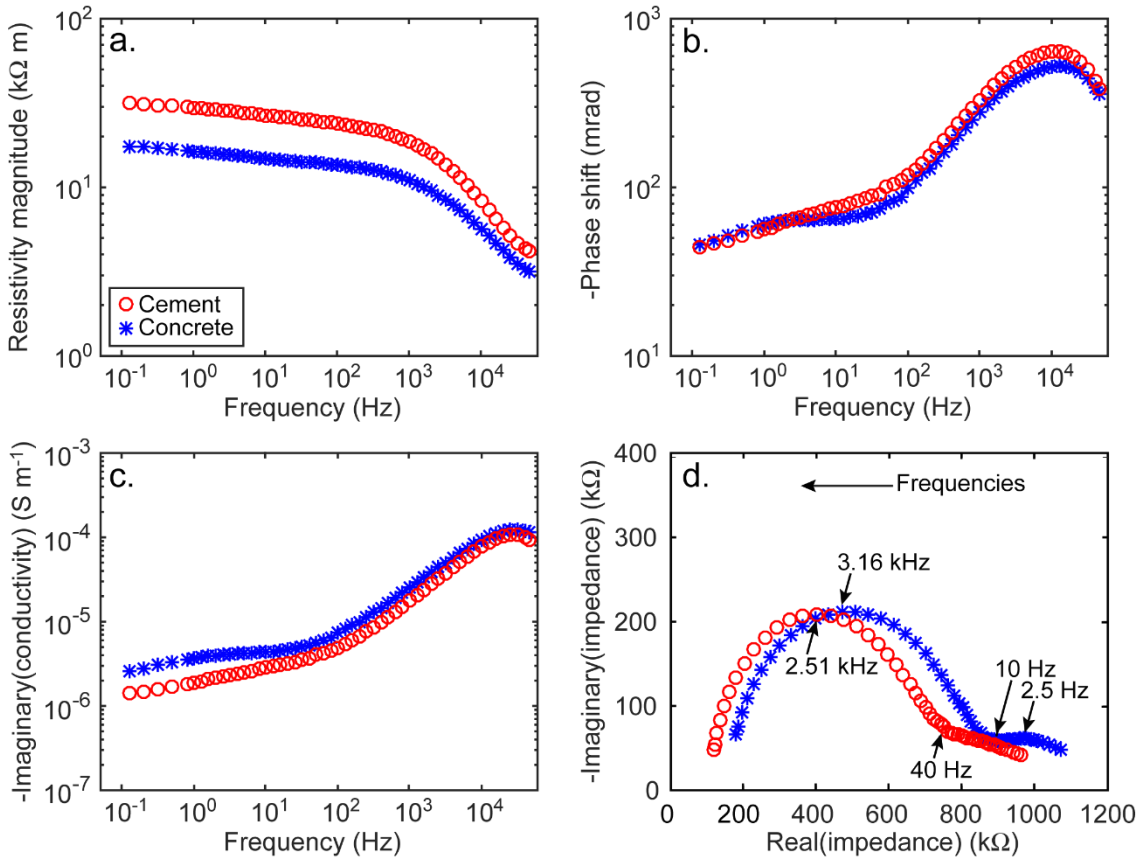

Fig. 9. Measured HCP and concrete SIP spectra (symbols).

In the absence of surface or internal (for metallic conductors or semi-conductors) conductivity effects, the electrical formation factor *F* inferred from Archie's first law [141] is a key geophysical parameter to relate the sample resistivity to its petrophysical properties when the sample is not completely dried [142-144]. However, for some minerals such as montmorillonite and illite that have a high surface conductivity due to

their high surface charge and specific surface area, resistivity measurements should be carried out at a sufficiently high salinity (typically ≥ 0.1 M) to neglect surface conductivity effects and obtain *F* [46, 93, 116, 143, 145-147]. In our study, we can expect a relatively high surface conductivity of cementitious materials due to the C-S-H presence and the relatively low salinity of the bulk pore water. However, we cannot increase the pore water salinity of the samples to obtain *F* because this would introduce disequilibrium conditions and associated degradation. In addition, for heterogeneous materials such as natural carbonates in partially water-saturated conditions, Archie's law may have a large uncertainty due to considerable variations in texture and pore geometry [148]. The apparent electrical formation factor defined by

$$F_a = \frac{\rho}{\rho_f}, \tag{13}$$

where ρ is the sample resistivity (not to be confounded with the apparent dry density) and ρ_f is the bulk water resistivity, can be calculated to obtain the lowest possible value of the (intrinsic) electrical formation factor [43, 117, 144]. Using Eq. (13) and the measured sample resistivity magnitude for frequencies below 100 Hz for ρ and the measured container water resistivity for ρ_f (11.6 Ω m), we obtained very high values for F_a, in the order of 2400 for HCP and 1390 for concrete. Many studies have reported considerably lower values for the intrinsic electrical formation factor *F* of soils and rocks, ranging from 2.5 to 198 for quartz, shaly sands, and sandstones [144, 149, 150]. The electrical formation factors of our cementitious samples are therefore extremely high.

When it is assumed that $F_a = F$ ($F_a \leq F$), the extremely high electrical formation factors can be interpreted by Archie's first law

$$F = \phi_c^{-m}, \tag{14}$$

where *m* is the cementation exponent associated with the particle shape. Using Eq. (14), the measured HCP and concrete porosities for ϕ_c (~25% and 12.5%, respectively), and the values of F_a previously shown, we obtained *m* values equal to 5.6 and 3.5 for HCP and concrete, respectively ($m = -\log F_a / \log \phi_c$). The *m* value of HCP may be too high considering the dimensions of C-S-H particles constituting cement. Indeed, using the typical dimensions of C-S-H particles reported in Gauffinet et al. [102] (60×50×5 nm^3), the theoretical cementation exponent can be calculated using the following equation for disk-shaped particles:

$$m = \frac{5 - 3L}{3\left(1 - L^2\right)}, \tag{15}$$

where

$$L = \frac{1 + e_c^{\,2}}{e_c^{\,3}}\left(e_c - \tan^{-1} e_c\right), \tag{16}$$

and

$$e_c = \sqrt{\left(d_p / h_p\right)^2 - 1}, \tag{17}$$

with *L* being the depolarization coefficient of the particle and e_c being its eccentricity [116, 151, 152]. Using Eqs. (15)-(17) and taking a diameter of 60 nm for d_p and a thickness of 5 nm for h_p, we obtained a theoretical *m* value of 3.5 for C-S-H, which is higher than the *m* values around 2 for most grains (comprised between 1.5 and 2.5 [143, 153]) and similar to the *m* values of clays such as montmorillonite [93, 116, 143, 147]. The high cementation exponent of 5.6 obtained for HCP from the experimental data seems to suggest that a significant part of the HCP porosity is not electrically connected.

Using Eq. (14), the theoretical *m* value (3.5), and the estimated *F* value (2400) for HCP, an electrically connected porosity of ~11% is obtained. The actual value may be even lower considering a higher intrinsic formation factor in the case of surface conductivity effects. Therefore, we estimated that 44% maximum of the total HCP porosity (11/25) is electrically connected. The use of the electrical formation factor therefore indicates that a significant part of the cement porosity is not electrically connected. Because the sample resistivity is controlled by the C-S-H content, it seems reasonable to suppose that the lamellar shape of C-S-H particles (explaining their high cementation exponent and resulting long current paths) and their very resistive interlayer spaces (explaining their low electrically connected porosity) are responsible for the extremely high resistivity of HCP and concrete. It should be noted that the analysis relies on the assumption that the pore space can actually be separated into a "connected" and a "disconnected" pore space (for electrical conduction), and that eq. (14) is a good description of the relationship between formation factor and connected porosity. However, the realistic functional behaviour may be more complex than suggested by eq. (14), introducing some uncertainty into the actual numbers [148]. Since our main conclusion (a significant fraction of porosity does not participate in electrical conduction) is not affected, and well-established theories are missing, we consider eq. (14) sufficient at this stage.

4.2. Single bi-tube models

The modelling results obtained for the single bi-tube pore system (Fig. 8a) reproduce the magnitude and trends of the SIP measurements (Fig. 10) using the parameter values reported in Table 3 and Table 4 after manual calibration to measured data. In particular,

the decrease of the resistivity magnitude and the increase of the phase shift and imaginary conductivity with frequency are reasonably captured. The semi-circular shapes of the Nyquist plots were also reproduced by our model. For each sample, the simulated phase shift spectrum shows two distinct peaks: a low-frequency peak below 10 Hz due to membrane polarization and a high-frequency peak at ~1 kHz due to MW polarization (Fig. 10b). At the right edge of the spectrum, another increase of the simulated phase shift is indicated. This is due to the displacement currents in the pore water, i.e. to the water permittivity effect in Eq. (8). The MW peak matches the high-frequency range of the spectrum up to ~2 kHz. At low frequencies, membrane polarization causes a distinct peak, which is in the appropriate frequency range and of similar size (tens of mrad) as the measured data. The qualitative match indicates that membrane polarization may be a relevant process. Nevertheless, the measured phase shift spectra are flat for frequencies below 100 Hz and a quantitative match is not possible with a single bi-tube model, because the peak-like behaviour is inherent to the model.

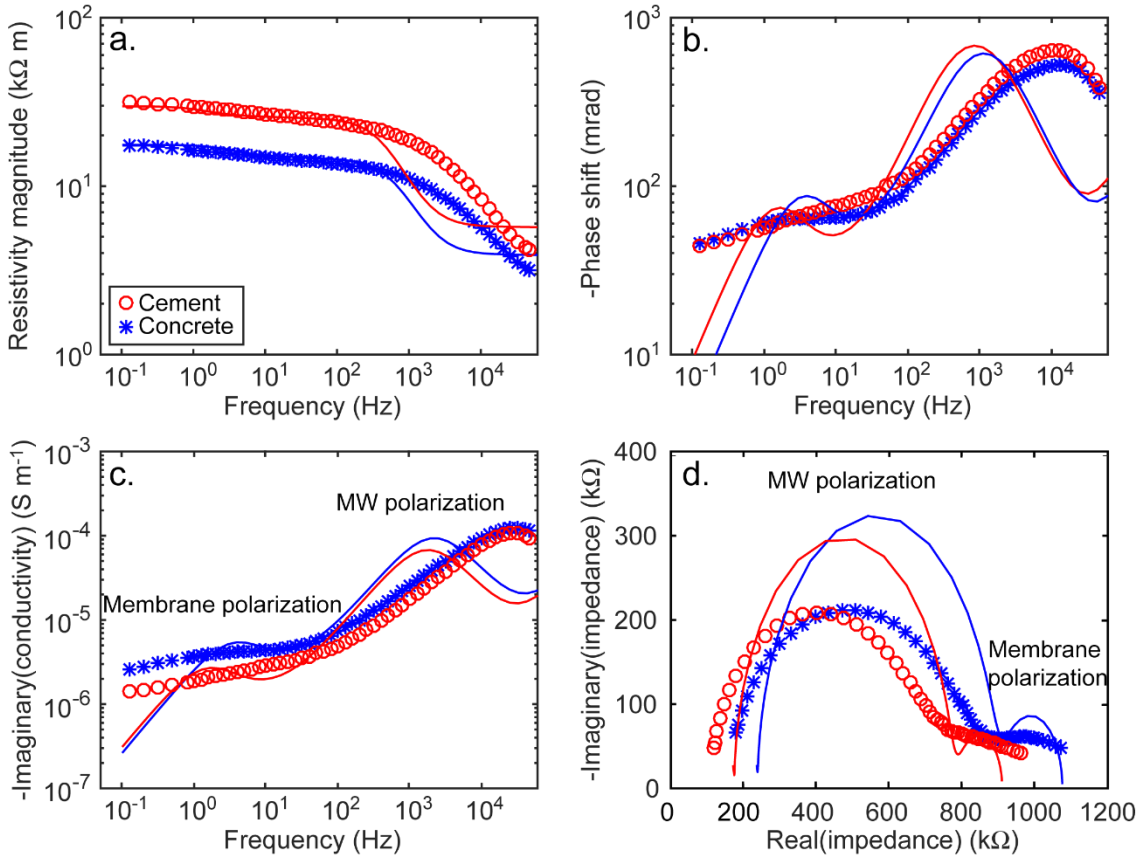

Fig. 10. Measured HCP and concrete SIP spectra (symbols) and simulation results using one bi-tube system (red line for HCP and blue line for concrete).

Table 4

Geometrical parameter values of the single bi-tube pore system.

Property	Symbol	Cement	Concrete
Pore 1 radius	R_1	0.15 μm	0.15 μm
Pore 2 radius	R_2	3 nm	3.1 nm
Pore 1 length	L_1	45 μm	30 μm
Pore 2 length	L_2	110 nm	60 nm
Matrix radius	R_0	3.6 μm	3 μm

The pore radii used to compute the resistivity magnitude and phase shift spectra (0.15 μm for the wide pore and ~3 nm for the narrow pore, Table 4) are in the same order of

magnitude as the mean values reported from MIP measurements (~0.5 µm and 6.5 nm, Fig. 1). However, MIP measurements should be taken with caution because they only probe pore-throat sizes larger than 7 nm [154, 155] and thus only 25 to 30% of the total porosity of our samples (Fig. 1). In addition, MIP determines the largest entrance to a pore and not the actual pore size [155]. Therefore, in reality, pore radii may be smaller than those inferred from MIP and thus closer to the values inferred from our computations. In the models, the wide pore lengths of 45 and 30 µm for HCP and concrete, respectively, control the frequency position of the peaks of the phase shift for low frequencies (membrane polarization). To simulate the observed high resistivity magnitudes of HCP and concrete, we chose a large radius of the non-conducting matrix ≥ 3 µm (Table 4), which decreases the connected porosity and increases the resistivity (Eq. (6) and Fig. 7a). The connected porosities inferred from the pore radius and length and the matrix radius are in the percent range for HCP and concrete. A smaller porosity was required for HCP to explain the higher resistivity magnitude (Fig. 10a). The estimated porosities are considerably smaller than the measured ones. This large underestimation of the porosity by the model may be due to the assumption that all the pores are connected and electrically conductive. As already discussed above, the fact that the estimated connected porosity obtained with Archie's first law is significantly smaller than the measured total porosity suggests that a significant part of the pore space may not participate in current transport. This statement should be considered as qualitative in view of the uncertainties associated with the use of Archie's first law, which may not be sufficient to describe the full complexity of the relationship between porosity and conductivity.

4.3. Bi-tube network models

2D network models where each single impedance corresponds to that of a bi-tube pore system (Fig. 8b) were used to compute the resistivity of the cement-based materials (Fig. 11) [83]. Kirchhoff's law leads to a system of equations that can be solved numerically to obtain the impedance of the entire network. Each bi-tube pore system considers membrane polarization as discussed in the previous section. In principle, any combination of pore radii and lengths may be realized, but it is useful to describe the geometrical properties of the network by a reduced number of parameters. Stebner et al. [83] proposed a power-law relationship between pore radii and lengths and a parameterization that considers the ratio between the radius of the wide and narrow pore, amongst others. Here, we used a modified version with two dominant pore radii and lengths and chose a logarithmic Gaussian distribution with a defined width around the dominant values. In the network model, the MW polarization process was implemented in a slightly simplified form. Instead of considering it for every single impedance, it was computed using the dominant pore radii and lengths and Eqs. (7) to (10).

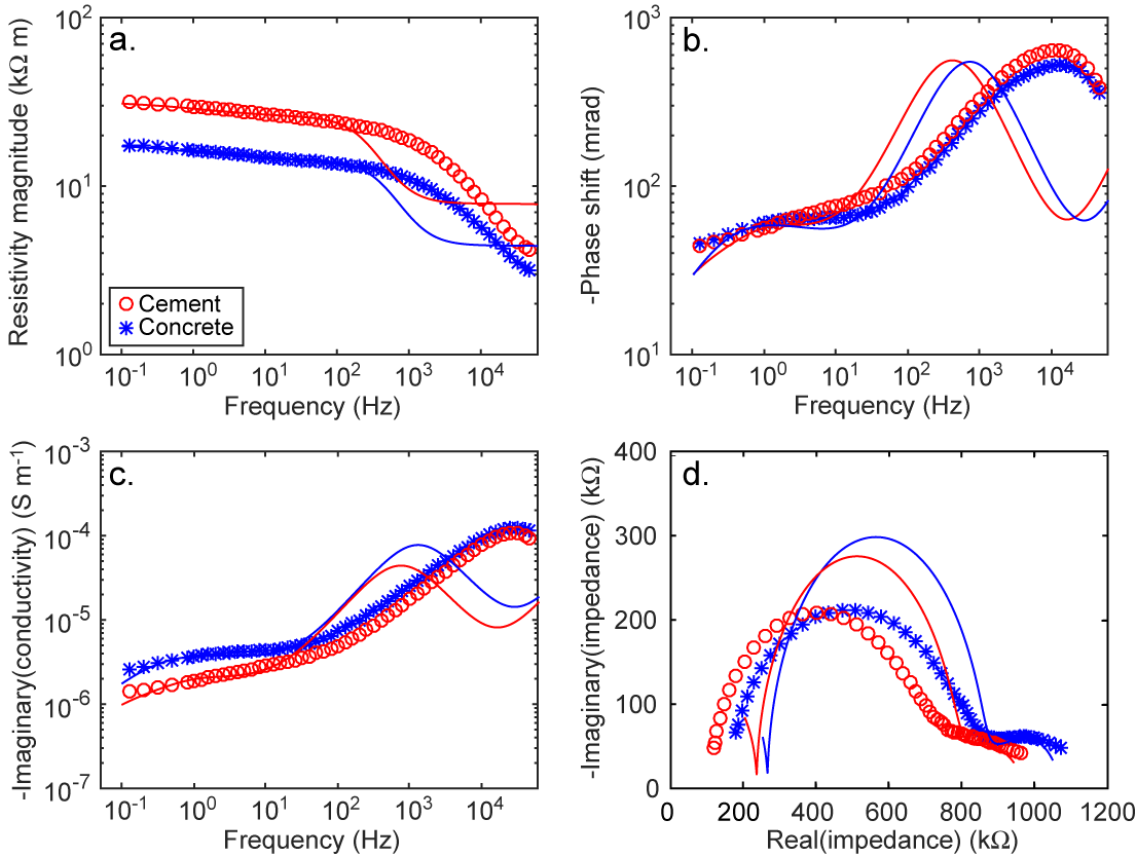

Fig. 11. Measured HCP and concrete SIP spectra (symbols) and simulation results using network bi-tube models (red line for HCP and blue line for concrete).

Compared to the computations of the bi-tube pore system, the modelled phase shift spectrum is smoother over the entire low-frequency range, and its shape as well as the imaginary conductivity and Nyquist plots for frequencies below 50 Hz are in better agreement with the measured data (Fig. 11). The geometrical parameter values after manual calibration to the measured SIP data using the mean pore radii and lengths from the single bi-tube systems are reported in Table 5. Pore radii inferred from the pore network models are smaller than the values inferred from MIP (Fig. 12 for HCP). Only electrically connected pores were included in the models. The connected porosity is still very low and in the percent range. To have a higher porosity in the model, it would have

been necessary to consider the interlayer space of the calcium-silicate-hydrate phase in the bi-tube pore network model (as explored in the following section), but this would have taken a lot more computational effort. This will be a topic of future work on SIP of cement.

Table 5

Geometrical parameter values (dominant pore radii and lengths) of the network models.

Property	Symbol	Cement	Concrete
Pore 1 radius	R_1	0.16 μm	0.16 μm
Pore 2 radius	R_2	3.1 nm	3.1 nm
Pore 1 length	L_1	67 μm	64 μm
Pore 2 length	L_2	83 nm	75 nm
Matrix radius	R_0	4.5 μm	3.4 μm
Distribution width	Λ	0.5	0.4

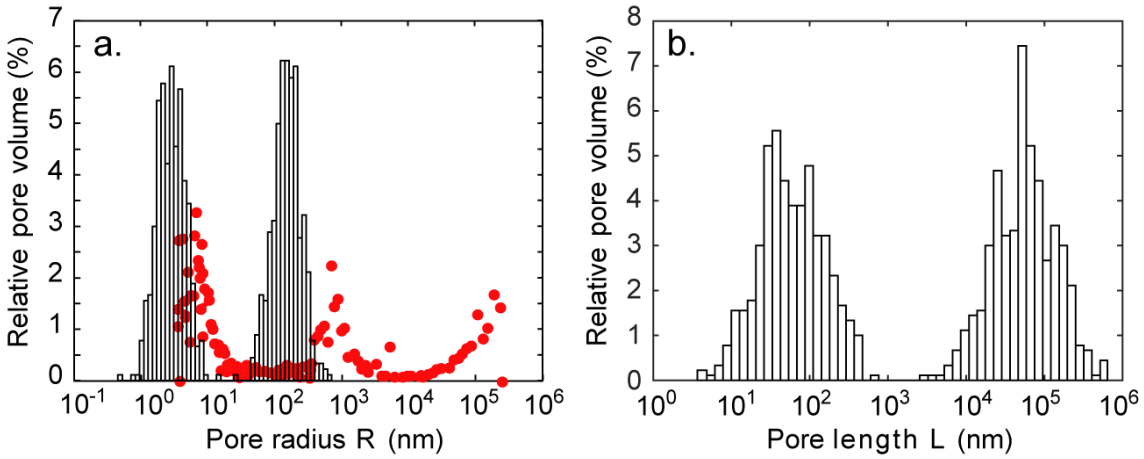

Fig. 12. a. Pore radius distribution and b. pore length distribution used in the network model to match the SIP measurements on HCP. Filled red circles are the pore radii measurements from MIP (Fig. 1). The distributions used in the network model to match the SIP measurements on concrete look similar and are not shown for brevity.

4.4. Two bi-tube systems in parallel

In this final set of simulations (Fig. 13), pores representing the interlayer spaces of C-S-H are now also included using a combination of two bi-tube systems in parallel. The radius of the pore is set to 1.3 Å in agreement with X-ray diffraction experiments showing that the thickness of the interlayer space is ~2.6 Å for fully hydrated C-S-H [106]. In the case of two bi-tube systems in parallel, the calculation of the resistivity ρ (in Ω m) from the simulated impedance Z (in Ω) requires an appropriate normalization ($\rho = Z \times A / L$). For a reasonable definition of resistivity, both bi-tube systems have to be normalized to the same length L and the cross-sectional area A has to be considered as well. In addition, it is desirable to control the relative volume of the two systems, which can also be included by appropriate normalization. Details of the calculations considered here are given in Appendix B.

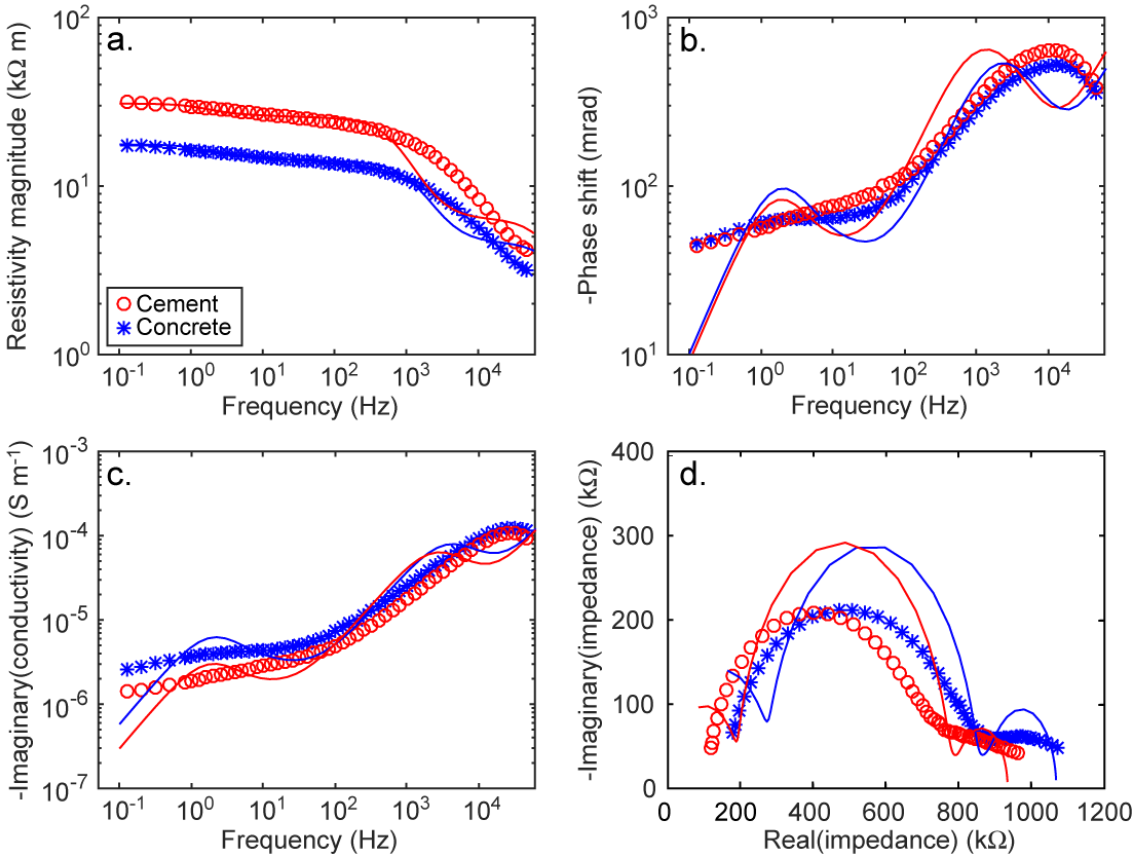

Fig. 13. Measured HCP and concrete SIP spectra (symbols) and simulation results using two bi-tube systems in parallel (red line for HCP and blue line for concrete).

The two bi-tube systems in parallel give the best agreement with the experimental SIP data for frequencies above 100 Hz (Fig. 13). The parameter values after manual calibration to the measured SIP data are given in Table 6. Compared to the previous simulations, the mean pore radii (0.2–0.25 μm for the wide pore and 5 nm for the narrow pore) are in closer agreement with the measured ones (~0.5 μm and 6.5 nm, Fig. 1). In addition, the model porosities, ~23.8% and 12.8% for HCP and concrete, respectively, better match the measured values (~25% and 12.5%).

It may seem unexpected that the two bi-tube system provides a better agreement with experimental data for frequencies above 10 Hz than the single bi-tube network model,

although the network model apparently has more free parameters. However, the network model also needs to be controlled by a finite (and not too large) number of parameters, and thus the possibilities in the current implementation are limited. Increasing the number of parameters of the network model in a reasonable way is not trivial, and might even complicate the task of trial-and-error fitting. Therefore, we consider the implementation of a full inversion based on a network model the next logical step rather than further increasing the number of manually controllable parameters.

Table 6

Geometrical parameter values of the two bi-tube systems in parallel.

Property	Symbol	Cement (1)	Cement (2)	Concrete (1)	Concrete (2)
Pore 1 radius	R_1	0.25 μm	1 μm	0.2 μm	1 μm
Pore 2 radius	R_2	5 nm	0.13 nm	5 nm	0.13 nm
Pore 1 length	L_1	42 μm	10 μm	42 μm	10 μm
Pore 2 length	L_2	80 nm	800 nm	80 nm	800 nm
Matrix radius	R_0	4.5 μm	1.4 μm	3.1 μm	1.92 μm
Volume fraction	w	0.5	0.5	0.5	0.5

5. Conclusions

We have carried out complex impedance measurements on low-pH cement paste and concrete in the low-frequency range (100 mHz–45 kHz) using a four-electrode set-up for spectral induced polarization (SIP) measurements. Resistivity magnitude and phase shift spectra between measured voltage and injected current have been obtained for these materials. We also have developed combined membrane and Maxwell-Wagner polarization models based on the membrane polarization models of Bücker and Hördt

[42], Bairlein et al. [82], Stebner et al. [83] and Bücker [84], which consider electrical double layer effects, porosity, bi-tube networks, and Maxwell-Wagner polarization, respectively, to describe these measurements. These models therefore consider the electrochemical and microstructural properties, namely, the zeta potential and the pore size and length, and the connected porosity of cement-based materials.

The measured resistivity magnitude and phase shift spectra of low-pH cement and concrete were very high. The resistivity magnitude was mostly above 10 kΩ m and the phase shift magnitude ranged from ~40 mrad at 100 mHz to ~625 mrad at 10 kHz. These observations were respectively attributed to (1) the presence of the insulating interlayer spaces in calcium-silicate-hydrate (C-S-H) particles, (2) membrane polarization between the micropores with high ion selectivity (calcium cation adsorption and sulfate anion repulsion) and the meso- and macropores with low ion selectivity, and (3) Maxwell-Wagner polarization between the solid and liquid phases. Our resistivity models were able to match the SIP measurements by considering pore sizes in relative agreement with and smaller than the values determined by mercury intrusion porosimetry (MIP). However, MIP only probes pore radii above 3.5 nm and 25–30% of the sample porosity. Therefore, in reality, pore radii may be smaller than those inferred from MIP and thus closer to the values inferred from our computations. It was also necessary to include very thin pores representing C-S-H interlayer spaces in our model to match the SIP measurements with a connected porosity corresponding to the measured value.

The present study shows that the pore structure and connected porosity of cementitious materials can be inferred from SIP. Our approach can therefore be used to monitor concrete stability in-situ. This is particularly interesting in the light of recent

developments in spectral electrical impedance tomography using borehole and surface electrodes to obtain the complex electrical resistivity distribution in the mHz to kHz frequency range [94, 95]. Such distributions could be used to obtain the spatial and temporal dynamics of the pore structure, connected porosity, and permeability. In the future, it would be very interesting to numerically solve the Poisson-Nernst-Planck equations to improve the accuracy of the resistivity models and consider polarization of steel reinforcement in concrete structures. Laboratory SIP studies for cement-based materials in partially water-saturated conditions, which are much closer to actual field conditions [156], should also be investigated.

Acknowledgments

The authors sincerely thank the editor Nemkumar Banthia and the two anonymous reviewers for their careful and constructive review of our manuscript. The research work of Philippe Leroy, Stéphane Gaboreau, Egon Zimmermann, Francis Claret, and Johan Alexander Huisman was supported by the Horizon 2020 CEBAMA project co-funded by the European Commission under the Euratom Research and Training Programme on Nuclear Energy (Contract Number: 662147). The research work of Andreas Hördt and Hermann Stebner was sponsored by the German Science foundation (grant Ho1506/23-1). Tapio Vehmas from VTT Technical Research Centre (Finland) is thanked for providing us the cement and concrete samples. Philippe Leroy warmly thanks Vanessa Montoya for providing him useful information on cementitious samples. The authors also thank Alba Valls, Andres Idiart and the ExCom members for their thorough review of the manuscript.

Appendix A. Membrane polarization model of Bücker and Hördt [42]

In this appendix, some parameters in Eq. (4) for calculating the normalized impedance of a bi-tube system are explained below:

$$\tilde{B} = \frac{\tilde{b}_{p1}}{\tilde{b}_{p2}}, \tag{A1}$$

$$A = \frac{L_1}{L_2}, \tag{A2}$$

$$\tilde{S}_i = \frac{\tilde{t}_{ni}}{\tilde{t}_{pi}}, \tag{A3}$$

$$\tilde{X}_i(\omega) = \frac{L_i}{2}\sqrt{\frac{j\omega}{2D_p\tilde{t}_{ni}\tilde{b}_{pi}}}, \tag{A4}$$

$$\tilde{t}_{p,ni} = \frac{\mu_{p,n}\tilde{b}_{p,ni}}{\mu_p\tilde{b}_{pi} + \mu_n\tilde{b}_{ni}}, \tag{A5}$$

where the cation diffusion coefficient D_p ($m^2\ s^{-1}$) is related to its mobility by the Nernst-Einstein equation

$$D_p = \frac{k_B T}{ez}\mu_p, \tag{A6}$$

where k_B is the Boltzmann's constant (~1.381×10^{-23} J K^{-1}), T is the temperature (K) and e is the electronic charge (~1.602×10^{-19} C). The normalized ion concentrations in the two pore types were calculated from their zeta potential ζ (V), radius R_i (m), and charge fraction in the Stern layer f_Q using:

$$\tilde{b}_{pi} = \frac{\bar{b}_{pi} - f_Q}{1 - f_Q}, \tag{A7}$$

$$\tilde{b}_{ni} = \bar{b}_{ni}, \tag{A8}$$

$$\bar{b}_{p,ni} = \frac{2}{R_i^2}\int_0^{R_i} b_{p,n}(r)\,r\,dr, \tag{A9}$$

$$b_{p,n}(r) = e^{\mp\frac{ez\psi(r)}{k_B T}}, \tag{A10}$$

$$\psi(r) = \zeta \frac{J_0(j\kappa r)}{J_0(j\kappa R_i)}, \tag{A11}$$

$$\kappa = \lambda_D^{-1} = \sqrt{\frac{2c_0 e z^2 F}{\varepsilon_{rf} \varepsilon_0 k_B T}}, \tag{A12}$$

where *r* is the radial coordinate from the pore center (m), ψ is the electrostatic potential in the EDL (V), J_0 is the zero order Bessel function, and κ is the inverse of the Debye length (m^{-1}). The quantity $\varepsilon_f = \varepsilon_{rf}\varepsilon_0$ is the fluid permittivity more thoroughly explained in section 3.2. It should be noted that the electrostatic potential in the tube can also be determined by numerically solving the Poisson-Boltzmann equation, which may be more accurate than using Eqs. (A11) and (A12) for nanopores exhibiting large zeta potentials (magnitude above 50 mV) and containing multivalent electrolytes [157]. Furthermore, Eqs. (A7) and (A8) were written for a negative surface charge, which is the most common case for minerals in contact with water in normal physico-chemical conditions (neutral pH and ionic strength below 1 M) [145, 158, 159]. However, when the surface charge is positive as in the case of cements with a high Ca/Si ratio (typically ≥ 1 [96, 105]) in contact with water, Eqs. (A7) and (A8) should be rewritten considering $\tilde{b}_{pi} = \bar{b}_{pi}$ and $\tilde{b}_{ni} = (\bar{b}_{ni} - f_Q)/(1 - f_Q)$.

Appendix B. Resistivity of two bi-tube systems in parallel

The two bi-tube systems in parallel (Fig. 8c) are each characterized by an impedance Z_a and Z_b, total length L_a and L_b, and cross-sectional area A_a and A_b. The total length of each bi-tube system equals the sum of the tube lengths and the cross-sectional area of each bi-tube system equals that of the insulating matrix cylinder. In order to calculate the resistivity of the two bi-tube systems in parallel, we first normalized the impedances to the same length *L*. The choice of the length itself is not critical, as it will cancel out when calculating the resistivity from the impedance. We may choose

$$L = \max(L_a, L_b) \tag{B1}$$

for the total system length. For the total cross-sectional area, we may simply give equal weight to the two bi-tube systems and use the sum of their two cross-sectional areas, i.e. $A = A_a + A_b$. However, as the radii of the insulating matrix may be very different, an equal weighting of the cross-sectional areas may lead to a complete dominance of one of them for the calculation of the impedance. Therefore, we introduced an additional parameter *V*, which controls the relative volumes (and thus the relative weights of the cross-sectional areas) of the two systems. We defined weights as

$$w_a = V; w_b = 1 - V\,, \tag{B2}$$

and the total cross-sectional area was calculated as the weighted sum of A_a and A_b:

$$A = w_a A_a + w_b A_b\,. \tag{B3}$$

The normalized and weighted impedance of each bi-tube system was calculated via:

$$\tilde{Z}_i = Z_i \frac{L}{L_i} \frac{w_i A_i}{A}. \tag{B4}$$

We then calculated the total impedance using the rules for parallel circuits:

$$Z = \left(\frac{1}{\tilde{Z}_a} + \frac{1}{\tilde{Z}_b} \right)^{-1} , \tag{B5}$$

and we finally obtained the resistivity of the two bi-tube systems in parallel through:

$$\rho = Z \frac{A}{L} . \tag{B6}$$

References

[1] J.W. Sandeman, Portland Cement Concrete, Minutes of the Proceedings of the Institution of Civil Engineers 54(1878) (1878) 251-263.

[2] H.F.W. Taylor, Cement Chemistry, Thomas Telford1997.

[3] S. Tsivilis, J. Tsantilas, G. Kakali, E. Chaniotakis, A. Sakellariou, The permeability of Portland limestone cement concrete, Cement Concrete Res 33(9) (2003) 1465-1471.

[4] F. Claret, S. Grangeon, A. Loschetter, C. Tournassat, W. De Nolf, N. Harker, F. Boulahya, S. Gaboreau, Y. Linard, X. Bourbon, A. Fernandez-Martinez, J. Wright, Deciphering mineralogical changes and carbonation development during hydration and ageing of a consolidated ternary blended cement paste, IUCrJ 5(2) (2018) 150-157.

[5] C. Cau Dit Coumes, S. Courtois, D. Nectoux, S. Leclercq, X. Bourbon, Formulating a low-alkalinity, high-resistance and low-heat concrete for radioactive waste repositories, Cement Concrete Res 36(12) (2006) 2152-2163.

[6] M. Codina, C. Cau-dit-Coumes, P. Le Bescop, J. Verdier, J.P. Ollivier, Design and characterization of low-heat and low-alkalinity cements, Cement Concrete Res 38(4) (2008) 437-448.

[7] B. Lothenbach, K. Scrivener, R.D. Hooton, Supplementary cementitious materials, Cement Concrete Res 41(12) (2011) 1244-1256.

[8] S. Gaboreau, D. Prêt, V. Montouillout, P. Henocq, J.-C. Robinet, C. Tournassat, Quantitative mineralogical mapping of hydrated low pH concrete, Cement and Concrete Composites 83 (2017) 360-373.

[9] A. Jenni, U. Mäder, C. Lerouge, S. Gaboreau, B. Schwyn, In situ interaction between different concretes and Opalinus Clay, Physics and Chemistry of the Earth, Parts A/B/C 70-71 (2014) 71-83.

[10] A. Dauzeres, G. Achiedo, D. Nied, E. Bernard, S. Alahrache, B. Lothenbach, Magnesium perturbation in low-pH concretes placed in clayey environment—solid characterizations and modeling, Cement Concrete Res 79 (2016) 137-150.

[11] C. Lerouge, S. Gaboreau, S. Grangeon, F. Claret, F. Warmont, A. Jenni, V. Cloet, U. Mäder, In situ interactions between Opalinus Clay and Low Alkali Concrete, Physics and Chemistry of the Earth, Parts A/B/C 99 (2017) 3-21.

[12] U. Mäder, A. Jenni, C. Lerouge, S. Gaboreau, S. Miyoshi, Y. Kimura, V. Cloet, M. Fukaya, F. Claret, T. Otake, M. Shibata, B. Lothenbach, 5-year chemico-physical evolution of concrete–claystone interfaces, Mont Terri rock laboratory (Switzerland), Swiss Journal of Geosciences 110(1) (2017) 307-327.

[13] J.L.G. Calvo, A. Hidalgo, C. Alonso, L.F. Luco, Development of low-pH cementitious materials for HLRW repositories Resistance against ground waters aggression, Cement Concrete Res 40(8) (2010) 1290-1297.

[14] T.T.H. Bach, C.C.D. Coumes, I. Pochard, C. Mercier, B. Revel, A. Nonat, Influence of temperature on the hydration products of low pH cements, Cement Concrete Res 42(6) (2012) 805-817.

[15] B. Lothenbach, G. Le Saout, M. Ben Haha, R. Figi, E. Wieland, Hydration of a low-alkali CEM III/B–SiO2 cement (LAC), Cement Concrete Res 42(2) (2012) 410-423.

[16] A. Dauzères, P. Le Bescop, C. Cau-Dit-Coumes, F. Brunet, X. Bourbon, J. Timonen, M. Voutilainen, L. Chomat, P. Sardini, On the physico-chemical evolution of low-pH and CEM I cement pastes interacting with Callovo-Oxfordian pore water under its in situ CO2 partial pressure, Cement Concrete Res 58 (2014) 76-88.

[17] B.W. Langan, K. Weng, M.A. Ward, Effect of silica fume and fly ash on heat of hydration of Portland cement, Cement Concrete Res 32(7) (2002) 1045-1051.

[18] V. Yogendran, B.W. Langan, M.N. Haque, M.A. Ward, Silica Fume in High-Strength Concrete, Materials Journal 84(2) (1987) 124-129.

[19] M. Mazloom, A.A. Ramezanianpour, J.J. Brooks, Effect of silica fume on mechanical properties of high-strength concrete, Cement and Concrete Composites 26(4) (2004) 347-357.

[20] C.S. Poon, S.C. Kou, L. Lam, Compressive strength, chloride diffusivity and pore structure of high performance metakaolin and silica fume concrete, Construction and Building Materials 20(10) (2006) 858-865.

[21] T. Nochaiya, W. Wongkeo, A. Chaipanich, Utilization of fly ash with silica fume and properties of Portland cement–fly ash–silica fume concrete, Fuel 89(3) (2010) 768-774.

[22] T.T.H. Bach, E. Chabas, I. Pochard, C. Cau Dit Coumes, J. Haas, F. Frizon, A. Nonat, Retention of alkali ions by hydrated low-pH cements: Mechanism and Na+/K+ selectivity, Cement Concrete Res 51 (2013) 14-21.

[23] J.L.G. Calvo, M.S. Moreno, M.C.A. Alonso, A.H. Lopez, J.G. Olmo, Study of the Microstructure Evolution of Low-pH Cements Based on Ordinary Portland Cement (OPC) by Mid- and Near-Infrared Spectroscopy, and Their Influence on Corrosion of Steel Reinforcement, Materials 6(6) (2013) 2508-2521.

[24] U. Berner, D.A. Kulik, G. Kosakowski, Geochemical impact of a low-pH cement liner on the near field of a repository for spent fuel and high-level radioactive waste, Physics and Chemistry of the Earth, Parts A/B/C 64 (2013) 46-56.

[25] N.C.M. Marty, O. Bildstein, P. Blanc, F. Claret, B. Cochepin, E.C. Gaucher, D. Jacques, J.E. Lartigue, S.H. Liu, K.U. Mayer, J.C.L. Meeussen, I. Munier, I. Pointeau, D.Y. Su, C.I. Steefel, Benchmarks for multicomponent reactive transport across a cement/clay interface, Computat Geosci 19(3) (2015) 635-653.

[26] O. Bildstein, F. Claret, Stability of Clay Barriers Under Chemical Perturbations, 6 (2015) 155-188.

[27] H. Vanhala, Mapping oil-contaminated sand and till with the spectral induced polarization (SIP) method, Geophys Prospect 45(2) (1997) 303-326.

[28] A. Binley, L.D. Slater, M. Fukes, G. Cassiani, Relationship between spectral induced polarization and hydraulic properties of saturated and unsaturated sandstone, Water Resources Research 41(12) (2005) n/a-n/a.

[29] C.A. Davis, E. Atekwana, E. Atekwana, L.D. Slater, S. Rossbach, M.R. Mormile, Microbial growth and biofilm formation in geologic media is detected with complex conductivity measurements, Geophysical Research Letters 33(18) (2006) n/a-n/a.

[30] A. Revil, N. Florsch, Determination of permeability from spectral induced polarization in granular media, Geophys J Int 181(3) (2010) 1480-1498.

[31] A. Kemna, A. Hordt, N. Klitzsch, Special Issue on Induced Polarization for Near-surface Investigations Foreword, Near Surf Geophys 10(6) (2012) 451-452.

[32] A. Weller, L. Slater, Salinity dependence of complex conductivity of unconsolidated and consolidated materials: Comparisons with electrical double layer models, Geophysics 77(5) (2012) D185-D198.

[33] A. Binley, S.S. Hubbard, J.A. Huisman, A. Revil, D.A. Robinson, K. Singha, L.D. Slater, The emergence of hydrogeophysics for improved understanding of subsurface processes over multiple scales, Water Resources Research 51(6) (2015) 3837-3866.

[34] P. Leroy, S. Li, D. Jougnot, A. Revil, Y. Wu, Modeling the evolution of complex conductivity during calcite precipitation on glass beads, Geophys J Int 209(1) (2017) 123–140.

[35] W.H. Pelton, S.H. Ward, P.G. Hallof, W.R. Sill, P.H. Nelson, Mineral Discrimination and Removal of Inductive Coupling with Multifrequency-Ip, Geophysics 43(3) (1978) 588-609.

[36] F. Borner, M. Gruhne, J. Schon, Contamination Indications Derived from Electrical-Properties in the Low-Frequency Range, Geophys Prospect 41(1) (1993) 83-98.

[37] T.L. Chelidze, Y. Gueguen, C. Ruffet, Electrical spectroscopy of porous rocks: a review - II. Experimental results and interpretation, Geophys J Int 137(1) (1999) 16-34.

[38] E. Zimmermann, A. Kemna, J. Berwix, W. Glaas, H.M. Munch, J.A. Huisman, A high-accuracy impedance spectrometer for measuring sediments with low polarizability, Meas Sci Technol 19(10) (2008).

[39] D.P. Lesmes, F.D. Morgan, Dielectric spectroscopy of sedimentary rocks, J Geophys Res-Sol Ea 106(B7) (2001) 13329-13346.

[40] P. Leroy, A. Revil, A. Kemna, P. Cosenza, A. Ghorbani, Complex conductivity of water-saturated packs of glass beads, Journal of Colloid and Interface Science 321(1) (2008) 103-117.

[41] A. Revil, M. Skold, Salinity dependence of spectral induced polarization in sands and sandstones, Geophys J Int 187(2) (2011) 813-824.

[42] M. Bücker, A. Hördt, Analytical modelling of membrane polarization with explicit parametrization of pore radii and the electrical double layer, Geophys J Int 194(2) (2013) 804-813.

[43] Q.F. Niu, A. Revil, M. Saidian, Salinity dependence of the complex surface conductivity of the Portland sandstone, Geophysics 81(2) (2016) D125-D140.

[44] A.D. Hollingsworth, D.A. Saville, A broad frequency range dielectric spectrometer for colloidal suspensions: cell design, calibration, and validation, Journal of Colloid and Interface Science 257(1) (2003) 65-76.

[45] J.A. Huisman, E. Zimmermann, O. Esser, F.-H. Haegel, A. Treichel, H. Vereecken, Evaluation of a novel correction procedure to remove electrode impedance effects from broadband SIP measurements, J Appl Geophys 135 (2016) 466-473.

[46] P. Leroy, M. Weigand, G. Mériguet, E. Zimmermann, C. Tournassat, F. Fagerlund, A. Kemna, J.A. Huisman, Spectral induced polarization of Na-montmorillonite dispersions, Journal of Colloid and Interface Science 505 (2017) 1093-1110.

[47] J. Kijlstra, R.A.J. Wegh, H.P. Vanleeuwen, Impedance Spectroscopy of Colloids, J Electroanal Chem 366(1-2) (1994) 37-42.

[48] M.C. Tirado, F.J. Arroyo, A.V. Delgado, C. Grosse, Measurement of the low-frequency dielectric properties of colloidal suspensions: Comparison between different methods, Journal of Colloid and Interface Science 227(1) (2000) 141-146.

[49] P. Xie, P. Gu, Z. Xu, J.J. Beaudoin, A rationalized a.c. impedence model for microstructural characterization of hydrating cement systems, Cement Concrete Res 23(2) (1993) 359-367.

[50] S.S. Yoon, H.C. Kim, R.M. Hill, The dielectric response of hydrating porous cement paste, Journal of Physics D: Applied Physics 29(3) (1996) 869-875.

[51] X. Hu, C. Shi, X. Liu, J. Zhang, G. de Schutter, A review on microstructural characterization of cement-based materials by AC impedance spectroscopy, Cement and Concrete Composites 100 (2019) 1-14.

[52] B.J. Christensen, T. Coverdale, R.A. Olson, S.J. Ford, E.J. Garboczi, H.M. Jennings, T.O. Mason, Impedance Spectroscopy of Hydrating Cement-Based Materials: Measurement, Interpretation, and Application, J Am Ceram Soc 77(11) (1994) 2789-2804.

[53] I.L. Ai-Qadi, O.A. Hazim, W. Su, S.M. Riad, Dielectric Properties of Portland Cement Concrete at Low Radio Frequencies, J Mater Civil Eng 7(3) (1995) 192-198.

[54] A. Robert, Dielectric permittivity of concrete between 50 Mhz and 1 Ghz and GPR measurements for building materials evaluation, J Appl Geophys 40(1-3) (1998) 89-94.

[55] N.E. Hager, R.C. Domszy, Monitoring of cement hydration by broadband time-domain-reflectometry dielectric spectroscopy, J Appl Phys 96(9) (2004) 5117-5128.

[56] G. Dey, A. Ganguli, B. Bhattacharjee, Electrical Conductivity, Dielectric Permittivity, and Degree of Saturation of Cement Mortar at Low Radio Frequencies, J Test Eval 47(4) (2019) 20170074.

[57] I.L.H. Hansson, C.M. Hansson, Electrical resistivity measurements of Portland cement based materials, Cement Concrete Res 13(5) (1983) 675-683.

[58] P. Gu, P. Xie, J.J. Beaudoin, R. Brousseau, A.C. impedance spectroscopy (II): Microstructural characterization of hydrating cement-silica fume systems, Cement Concrete Res 23(1) (1993) 157-168.

[59] M. Cabeza, P. Merino, A. Miranda, X.R. Nóvoa, I. Sanchez, Impedance spectroscopy study of hardened Portland cement paste, Cement Concrete Res 32(6) (2002) 881-891.

[60] B. Díaz, L. Freire, P. Merino, X.R. Nóvoa, M.C. Pérez, Impedance spectroscopy study of saturated mortar samples, Electrochim Acta 53(25) (2008) 7549-7555.

[61] J.M. Cruz, I.C. Fita, L. Soriano, J. Payá, M.V. Borrachero, The use of electrical impedance spectroscopy for monitoring the hydration products of Portland cement mortars with high percentage of pozzolans, Cement Concrete Res 50 (2013) 51-61.

[62] W.J. McCarter, H.M. Taha, B. Suryanto, G. Starrs, Two-point concrete resistivity measurements: interfacial phenomena at the electrode–concrete contact zone, Measurement Science and Technology 26(8) (2015) 085007.

[63] S.J. Ford, T.O. Mason, B.J. Christensen, R.T. Coverdale, H.M. Jennings, E.J. Garboczi, Electrode configurations and impedance spectra of cement pastes, J Mater Sci Technol 30 (1995) 1217-1224.

[64] P. Xie, P. Gu, J.J. Beaudoin, Contact capacitance effect in measurement of a.c. impedance spectra for hydrating cement systems, Journal of Materials Science and Technology 31 (1996) 144-149.

[65] B. Díaz, X.R. Nóvoa, M.C. Pérez, Study of the chloride diffusion in mortar: A new method of determining diffusion coefficients based on impedance measurements, Cement and Concrete Composites 28(3) (2006) 237-245.

[66] J.M. Torrents, P. Juan-García, A. Aguado, Electrical impedance spectroscopy as a technique for the surveillance of civil engineering structures: considerations on the galvanic insulation of samples, Measurement Science and Technology 18(7) (2007) 1958-1962.

[67] I. Sánchez, X.R. Nóvoa, G. de Vera, M.A. Climent, Microstructural modifications in Portland cement concrete due to forced ionic migration tests. Study by impedance spectroscopy, Cement Concrete Res 38(7) (2008) 1015-1025.

[68] D. Smyl, M. Hallaji, A. Seppänen, M. Pour-Ghaz, Quantitative electrical imaging of three-dimensional moisture flow in cement-based materials, International Journal of Heat and Mass Transfer 103 (2016) 1348-1358.

[69] D. Smyl, R. Rashetnia, A. Seppänen, M. Pour-Ghaz, Can Electrical Resistance Tomography be used for imaging unsaturated moisture flow in cement-based materials with discrete cracks?, Cement Concrete Res 91 (2017) 61-72.

[70] A. Revil, P. Leroy, Constitutive equations for ionic transport in porous shales, J Geophys Res-Sol Ea 109(B03208) (2004) 1-19.

[71] E. Samson, J. Marchand, Modeling the transport of ions in unsaturated cement-based materials, Comput Struct 85(23-24) (2007) 1740-1756.

[72] K. Krabbenhøft, J. Krabbenhøft, Application of the Poisson–Nernst–Planck equations to the migration test, Cement Concrete Res 38(1) (2008) 77-88.

[73] M. Aguayo, P. Yang, K. Vance, G. Sant, N. Neithalath, Electrically driven chloride ion transport in blended binder concretes: Insights from experiments and numerical simulations, Cement Concrete Res 66 (2014) 1-10.

[74] P. Yang, G. Sant, N. Neithalath, A refined, self-consistent Poisson-Nernst-Planck (PNP) model for electrically induced transport of multiple ionic species through concrete, Cement and Concrete Composites 82 (2017) 80-94.

[75] C.A.J. Appelo, Solute transport solved with the Nernst-Planck equation for concrete pores with 'free' water and a double layer, Cement Concrete Res 101 (2017) 102-113.

[76] D.J. Marshall, T.R. Madden, Induced Polarization, a Study of Its Causes, Geophysics 24(4) (1959) 790-816.

[77] V.W. Buchheim, G. Irmer, Zur Theorie der induzierten galvanischen Polarisation in Festkörpern mit elektrolytischer Porenfüllung, Gerlands Beiträge zur Geophysik 88(1) (1979) 53-72.

[78] K. Titov, V. Komarov, V. Tarasov, A. Levitski, Theoretical and experimental study of time domain-induced polarization in water-saturated sands, J Appl Geophys 50(4) (2002) 417-433.

[79] V.Y. Zadorozhnaya, M. Hauger, Mathematical Modeling of Membrane Polarization Occurring in Rocks Due to Applied Electrical Field, Izvestiya, Physics of the Solid Earth 45(12) (2009) 1038-1054.

[80] J. Volkmann, N. Klitzsch, Frequency-Dependent Electric Properties of Microscale Rock Models for Frequencies from One Millihertz to Ten Kilohertz, Vadose Zone J 9(4) (2010) 858.

[81] M. Bücker, A. Hördt, Long and short narrow pore models for membrane polarization, Geophysics 78(6) (2013) E299-E314.

[82] K. Bairlein, M. Bücker, A. Hördt, B. Hinze, Temperature dependence of spectral induced polarization data: experimental results and membrane polarization theory, Geophys J Int 205(1) (2016) 440-453.

[83] H. Stebner, M. Halisch, A. Hördt, Simulation of membrane polarization of porous media with impedance networks, Near-surface geophysics 15 (2017) 563-578.

[84] M. Bücker, Pore-scale modelling of induced-polarization mechanisms in geologic materials, Department of Geophysics, University of Bonn, Bonn, Germany, 2017.

[85] J.C. Maxwell, A Treatise on Electricity and Magnetism, third edition ed., Oxford University Press, London, 1892.

[86] K.W. Wagner, Erklarung der Dielektrischen Nachwirkungsvorgange auf Grund Maxwellscher Vorstellung, Arch. Elektrotech. 2 (1914) 371–387.

[87] A.J. Allen, J.J. Thomas, H.M. Jennings, Composition and density of nanoscale calcium–silicate–hydrate in cement, Nat Mater 6(4) (2007) 311-316.

[88] S. Gaboreau, D. Prêt, E. Tinseau, F. Claret, D. Pellegrini, D. Stammose, 15 years of in situ cement–argillite interaction from Tournemire URL: Characterisation of the multi-scale spatial heterogeneities of pore space evolution, Appl Geochem 26(12) (2011) 2159-2171.

[89] S. Gaboreau, J.-C. Robinet, D. Prêt, Optimization of pore-network characterization of a compacted clay material by TEM and FIB/SEM imaging, Micropor Mesopor Mat 224 (2016) 116-128.

[90] E.W. Washburn, The Dynamics of Capillary Flow, Physical Review 17(3) (1921) 273-283.

[91] W.H. Pelton, W.R. Sill, B.D. Smith, Interpretation of complex resistivity and dielectric data. Part I, Geophys Trans 29(4) (1983) 297-330.

[92] D. Jougnot, A. Ghorbani, A. Revil, P. Leroy, P. Cosenza, Spectral induced polarization of partially saturated clay-rocks: a mechanistic approach, Geophys J Int 180(1) (2010) 210-224.

[93] G. Okay, P. Leroy, A. Ghorbani, P. Cosenza, C. Camerlynck, J. Cabrera, N. Florsch, A. Revil, Spectral induced polarization of clay-sand mixtures: Experiments and modeling, Geophysics 79(6) (2014) E353-E375.

[94] Y. Zhao, E. Zimmermann, J.A. Huisman, A. Treichel, B. Wolters, S. Vanwaasen, A. Kemna, Broadband EIT borehole measurements with high phase accuracy using

numerical corrections of electromagnetic coupling effects, Meas Sci Technol 24(8) (2013).

[95] Y. Zhao, E. Zimmermann, J.A. Huisman, A. Treichel, B. Wolters, S. van Waasen, A. Kemna, Phase correction of electromagnetic coupling effects in cross-borehole EIT measurements, Meas Sci Technol 26(1) (2015) 1-11.

[96] H. Viallis-Terrisse, A. Nonat, J.C. Petit, Zeta-potential study of calcium silicate hydrates interacting with alkaline cations, Journal of Colloid and Interface Science 244(1) (2001) 58-65.

[97] J.J. Chen, J.J. Thomas, H.F.W. Taylor, H.M. Jennings, Solubility and structure of calcium silicate hydrate, Cement Concrete Res 34(9) (2004) 1499-1519.

[98] I.G. Richardson, The calcium silicate hydrates, Cement Concrete Res 38(2) (2008) 137-158.

[99] Y. Elakneswaran, T. Nawa, K. Kurumisawa, Electrokinetic potential of hydrated cement in relation to adsorption of chlorides, Cement Concrete Res 39(4) (2009) 340-344.

[100] A.J. Allen, R.C. Oberthur, D. Pearson, P. Schofield, C.R. Wilding, Development of the fine porosity and gel structure of hydrating cement systems, Philosophical Magazine B 56(3) (2006) 263-288.

[101] H.M. Jennings, Refinements to colloid model of C-S-H in cement: CM-II, Cement Concrete Res 38(3) (2008) 275-289.

[102] S. Gauffinet, E. Finot, E. Lesniewska, A. Nonat, Direct observation of the growth of calcium silicate hydrate on alite and silica surfaces by atomic force microscopy, Cr Acad Sci Ii A 327(4) (1998) 231-236.

[103] M. Grutzeck, A. Benesi, B. Fanning, Silicon-29 Magic Angle Spinning Nuclear Magnetic Resonance Study of Calcium Silicate Hydrates, J Am Ceram Soc 72(4) (1989) 665-668.

[104] X. Cong, R.J. Kirkpatrick, 29Si MAS NMR study of the structure of calcium silicate hydrate, Advanced Cement Based Materials 3(3-4) (1996) 144-156.

[105] J. Haas, A. Nonat, From C-S-H to C-A-S-H: Experimental study and thermodynamic modelling, Cement Concrete Res 68 (2015) 124-138.

[106] C. Roosz, S. Gaboreau, S. Grangeon, D. Prêt, V. Montouillout, N. Maubec, S. Ory, P. Blanc, P. Vieillard, P. Henocq, Distribution of Water in Synthetic Calcium Silicate Hydrates, Langmuir 32(27) (2016) 6794-6805.

[107] J.J. Thomas, H.M. Jennings, A.J. Allen, The surface area of hardened cement paste as measured by various techniques, Concrete Science and Engineering 1 (1999) 45-64.

[108] S. Grangeon, F. Claret, C. Roosz, T. Sato, S. Gaboreau, Y. Linard, Structure of nanocrystalline calcium silicate hydrates: insights from X-ray diffraction, synchrotron X-ray absorption and nuclear magnetic resonance, J Appl Crystallogr 49(3) (2016) 771-783.

[109] L. Nachbaur, P.C. Nkinamubanzi, A. Nonat, J.C. Mutin, Electrokinetic properties which control the coagulation of silicate cement suspensions during early age hydration, Journal of Colloid and Interface Science 202(2) (1998) 261-268.

[110] H. Viallis, P. Faucon, J.C. Petit, A. Nonat, Interaction between salts (NaCl, CsCl) and calcium silicate hydrates (C-S-H), Journal of Physical Chemistry B 103(25) (1999) 5212-5219.

[111] R. Kumar, B. Bhattacharjee, Porosity, pore size distribution and in situ strength of concrete, Cement Concrete Res 33(1) (2003) 155-164.

[112] C. Labbez, B. Jonsson, I. Pochard, A. Nonat, B. Cabane, Surface charge density and electrokinetic potential of highly charged minerals: Experiments and Monte Carlo simulations on calcium silicate hydrate, Journal of Physical Chemistry B 110(18) (2006) 9219-9230.

[113] P. Leroy, C. Tournassat, M. Bizi, Influence of surface conductivity on the apparent zeta potential of TiO2 nanoparticles, Journal of Colloid and Interface Science 356(2) (2011) 442-453.

[114] M. Heuser, G. Spagnoli, P. Leroy, N. Klitzsch, H. Stanjek, Electro-osmotic flow in clays and its potential for reducing clogging in mechanical tunnel driving, B Eng Geol Environ 71(4) (2012) 721-733.

[115] P. Leroy, D. Jougnot, A. Revil, A. Lassin, M. Azaroual, A double layer model of the gas bubble/water interface, Journal of Colloid and Interface Science 388 (2012) 243-256.

[116] P. Leroy, C. Tournassat, O. Bernard, N. Devau, M. Azaroual, The electrophoretic mobility of montmorillonite. Zeta potential and surface conductivity effects, Journal of Colloid and Interface Science 451 (2015) 21-39.

[117] S. Li, P. Leroy, F. Heberling, N. Devau, D. Jougnot, C. Chiaberge, Influence of surface conductivity on the apparent zeta potential of calcite, J Colloid Interface Sci 468 (2016) 262-75.

[118] R.J. Hunter, Zeta Potential in Colloid Science: Principles and Applications, Academic Press, New York, 1981.

[119] M. Von Smoluchowski, Zur theorie der elektrischen kataphorese und der oberflachenleitung, Physikalische Zeitschrift 6(17) (1905) 529-531.

[120] J.T.G. Overbeek, Theory of the relaxation effect in electrophoresis, Kolloide-Beihefte 54 (1943) 287–364.

[121] P.H. Wiersema, A.L. Loeb, J.T.G. Overbeek, Calculation of the Electrophoretic Mobility of a Spherical Colloid Particle, Journal of Colloid and Interface Science 22 (1966) 78-99.

[122] H.M. Jennings, A. Kumar, G. Sant, Quantitative discrimination of the nano-pore-structure of cement paste during drying: New insights from water sorption isotherms, Cement Concrete Res 76 (2015) 27-36.

[123] D. Hou, Z. Li, Molecular dynamics study of water and ions transport in nano-pore of layered structure: A case study of tobermorite, Micropor Mesopor Mat 195 (2014) 9-20.

[124] J.A. Greathouse, R.T. Cygan, J.T. Fredrich, G.R. Jerauld, Molecular Dynamics Simulation of Diffusion and Electrical Conductivity in Montmorillonite Interlayers, The Journal of Physical Chemistry C 120(3) (2016) 1640-1649.

[125] R.M. Tinnacher, M. Holmboe, C. Tournassat, I.C. Bourg, J.A. Davis, Ion adsorption and diffusion in smectite: Molecular, pore, and continuum scale views, Geochimica Et Cosmochimica Acta 177 (2016) 130-149.

[126] A.V. Delgado, F. Gonzalez-Caballero, R.J. Hunter, L.K. Koopal, J. Lyklema, Measurement and interpretation of electrokinetic phenomena, Journal of Colloid and Interface Science 309(2) (2007) 194-224.

[127] P. Leroy, N. Devau, A. Revil, M. Bizi, Influence of surface conductivity on the apparent zeta potential of amorphous silica nanoparticles, Journal of Colloid and Interface Science 410 (2013) 81-93.

[128] I.S. Bouhaik, P. Leroy, P. Ollivier, M. Azaroual, L. Mercury, Influence of surface conductivity on the apparent zeta potential of TiO2 nanoparticles: Application to the

modeling of their aggregation kinetics, Journal of Colloid and Interface Science 406 (2013) 75-85.

[129] L. Cary, H. Pauwels, P. Ollivier, G. Picot, P. Leroy, B. Mougin, G. Braibant, J. Labille, Evidence for TiO2 nanoparticle transfer in a hard-rock aquifer, J Contam Hydrol 179 (2015) 148-159.

[130] M. Codina, Les bétons bas pH - Formulation, caractérisation et étude à long terme, Sciences de l'ingénieur [physics], Institut National des Sciences Appliquees, Toulouse, France, 2007, p. 167.

[131] A. Revil, Ionic diffusivity, electrical conductivity, membrane and thermoelectric potentials in colloids and granular porous media: A unified model, Journal of Colloid and Interface Science 212(2) (1999) 503-522.

[132] V.C. Wagner, Die Oberflächenspannung verdünnter Elektrolytlösungen, Physik Zeitschrift 25 (1924) 474.

[133] O.A.L. de Lima, M.M. Sharma, A generalized Maxwell-Wagner theory for membrane polarization in shaly sands, Geophysics 57(3) (1992) 431-440.

[134] A. Hördt, K. Bairlein, M. Bücker, H. Stebner, Geometrical constraints for membrane polarization, Near-surface Geophysics 15 (2017) 579-592.

[135] G.R. Olhoeft, Electrical properties of rocks, in: W.R.J. Y. S. Touloukian, and R. F. Roy (Ed.), Physical properties of rocks and minerals, McGraw-Hill, New York, 1981, pp. 257–339.

[136] D.R. Lide, CRC Handbook of Chemistry and Physics CRC Press, Boca Raton, 1990.

[137] D.L. Parkhurst, C.A.J. Appelo, Description of Input and Examples for PHREEQC Version 3--a Computer Program for Speciation, Batch-reaction, One-dimensional Transport, and Inverse Geochemical Calculations, in: U.S.G.S. Reston (Ed.), U.S. Geological Survey Techniques and Methods, Book 6, Modeling Techniques, Denver, 2013, p. 497.

[138] F. Kohlrausch, Zurückführung der Siemens'sehen galvanischen Widerstandseinheit auf absolutes Maafs, in: J.A.B. Ergänzungsband VI (Ed.), ANNALEN DER PHYSIK UND CHEMIE, Leipzig, 1874.

[139] I. Pointeau, P. Reiller, N. Macé, C. Landesman, N. Coreau, Measurement and modeling of the surface potential evolution of hydrated cement pastes as a function of degradation, Journal of Colloid and Interface Science 300(1) (2006) 33-44.

[140] D. Lowke, C. Gehlen, The zeta potential of cement and additions in cementitious suspensions with high solid fraction, Cement Concrete Res 95 (2017) 195-204.

[141] G.E. Archie, The electrical resistivity log as an aid in determining some reservoir characteristics, Transactions of the American Institute of Mining, Metallurgical and Petroleum Engineers 146 (1942) 54-67.

[142] M.H. Waxman, L.J.M. Smits, Electrical conductivities in oil bearing shaly sands, Society of Petroleum Engineers Journal 8 (1968) 107-122.

[143] A. Revil, L.M. Cathles, S. Losh, J.A. Nunn, Electrical conductivity in shaly sands with geophysical applications, J Geophys Res-Sol Ea 103(B10) (1998) 23925-23936.

[144] A. Weller, L. Slater, S. Nordsiek, On the relationship between induced polarization and surface conductivity: Implications for petrophysical interpretation of electrical measurements, Geophysics 78(5) (2013) D315-D325.

[145] P. Leroy, A. Revil, A triple-layer model of the surface electrochemical properties of clay minerals, Journal of Colloid and Interface Science (2004) 371-380.

[146] P. Leroy, A. Revil, S. Altmann, C. Tournassat, Modeling the composition of the pore water in a clay-rock geological formation (Callovo-Oxfordian, France), Geochimica Et Cosmochimica Acta 71(5) (2007) 1087-1097.

[147] P. Leroy, A. Revil, A mechanistic model for the spectral induced polarization of clay materials, J Geophys Res-Sol Ea 114(B10202) (2009) 1-21.

[148] G.M. Hamada, A.A. Almajed, T.M. Okasha, A.A. Algathe, Uncertainty analysis of Archie's parameters determination techniques in carbonate reservoirs, Journal of Petroleum Exploration and Production Technology 3(1) (2012) 1-10.

[149] H.J. Vinegar, M.H. Waxman, Induced Polarization of Shaly Sands, Geophysics 49(8) (1984) 1267-1287.

[150] A. Revil, A. Binley, L. Mejus, P. Kessouri, Predicting permeability from the characteristic relaxation time and intrinsic formation factor of complex conductivity spectra, Water Resources Research 51(8) (2015) 6672-6700.

[151] K.S. Mendelson, M.H. Cohen, The effect of grain anisotropy on the electrical-properties of sedimentary-rocks, Geophysics 47(2) (1982) 257-263.

[152] P.N. Sen, Grain Shape Effects on Dielectric and Electrical-Properties of Rocks, Geophysics 49(5) (1984) 586-587.

[153] A. Revil, Thermal conductivity of unconsolidated sediments with geophysical applications, J Geophys Res-Sol Ea 105(B7) (2000) 16749-16768.

[154] A.B. Abell, K.L. Willis, D.A. Lange, Mercury Intrusion Porosimetry and Image Analysis of Cement-Based Materials, Journal of Colloid and Interface Science 211(1) (1999) 39-44.

[155] H. Giesche, Mercury Porosimetry: A General (Practical) Overview, Part Part Syst Char 23(1) (2006) 9-19.

[156] D.J. Smyl, Relating unsaturated electrical and hydraulic conductivity of cement-based materials, Australian Journal of Civil Engineering 16(2) (2018) 129-142.

[157] P. Leroy, A. Maineult, Exploring the electrical potential inside cylinders beyond the Debye-Hückel approximation: a computer code to solve the Poisson-Boltzmann equation for multivalent electrolytes, Geophys J Int 214(1) (2018) 58-69,.

[158] D. Sverjensky, Prediction of surface charge on oxides in salt solutions: Revisions for 1 : 1 (M+L-) electrolytes, Geochimica Et Cosmochimica Acta 69(2) (2005) 225-257.

[159] T. Hiemstra, W.H. Van Riemsdijk, On the relationship between charge distribution, surface hydration, and the structure of the interface of metal hydroxides, Journal of Colloid and Interface Science 301 (2006) 1-18.